

RESEARCH ARTICLE

10.1002/2013JB010708

Key Points:

- $^{40}\text{Ar}/^{39}\text{Ar}$ geochronology and thermochronology carried out
- Strong contrast cooling patterns for the NCC and YTC are identified
- Implications for dynamic setting of the eastern Asian continent are discussed

Supporting Information:

- Readme
- Appendix S1
- Appendix S2
- Appendix S3

Correspondence to:

F. Wang,
wangfei@mail.iggcas.ac.cn

Citation:

Wang, F., Q. Wang, W. Lin, L. Wu, W. Shi, H. Feng, and R. Zhu (2014), $^{40}\text{Ar}/^{39}\text{Ar}$ geochronology of the North China and Yangtze Cratons: New constraints on Mesozoic cooling and cratonic destruction under East Asia, *J. Geophys. Res. Solid Earth*, 119, 3700–3721, doi:10.1002/2013JB010708.

Received 22 SEP 2013

Accepted 13 MAR 2014

Accepted article online 20 MAR 2014

Published online 21 APR 2014

$^{40}\text{Ar}/^{39}\text{Ar}$ geochronology of the North China and Yangtze Cratons: New constraints on Mesozoic cooling and cratonic destruction under East Asia

Fei Wang¹, Qinchen Wang¹, Wei Lin¹, Lin Wu¹, Wenbei Shi¹, Huile Feng¹, and Rixiang Zhu¹¹State Key Laboratory of Lithospheric Evolution, Institute of Geology and Geophysics, Chinese Academy of Sciences, Beijing, China

Abstract Lithospheric destruction of the North China Craton (NCC) is a prominent phenomenon during the Mesozoic, but the timing and process are still in dispute. Furthermore, whether the Yangtze Craton (YTC) was also destructed is controversial. Twenty samples collected from the NCC and YTC were subjected to high-resolution $^{40}\text{Ar}/^{39}\text{Ar}$ geochronological and thermochronological studies. Average cooling rates of 450–150°C were estimated, showing that a rapid cooling event ($\sim 12^\circ\text{C}/\text{Ma}$) occurred on the NCC but not on the YTC during the Late Mesozoic. Crustal thickness can be roughly estimated by using pure conductive cooling showing that the crust of the NCC in the Jurassic was thicker than in the Cretaceous. Nonlinear cooling histories and cooling rates obtained by using multidomain diffusion theory show that the upper crusts of NCC and YTC had different cooling patterns during the Mesozoic. Combined with the sedimentation rates on the NCC, we argue that lithospheric thinning of the NCC began in the northern portion at ~ 140 – 135 Ma and peaked in the central and eastern portions at ~ 125 – 100 Ma, at a cooling rate of $\sim 9.6^\circ\text{C}/\text{Ma}$. In contrast, the YTC cooled gently during 200–75 Ma at a rate of $\sim 1.2^\circ\text{C}/\text{Ma}$, implying that the lithospheric thinning did not happen there during this time. Pure conductive cooling suggests that the crust of the YTC in the Late Triassic was thicker than the NCC in the Cretaceous; therefore, we argue that the lithospheric destruction in the YTC might have occurred after ~ 75 Ma.

1. Introduction

The North China Craton (NCC) and Yangtze Craton (YTC) dominate the eastern Asian continent (Figure 1a) and are crucial for the understanding of the dynamic evolution of the lithosphere. The NCC is the only craton on Earth that has been reactivated and destructed [Gao *et al.*, 2002; Zheng *et al.*, 2007] resulting in lithospheric thinning from more than 150 km to less than 80 km, which most likely happened in the Mesozoic [e.g., Griffin *et al.*, 1992; Gao *et al.*, 2002; Zhang *et al.*, 2003; Wilde *et al.*, 2003; Xu *et al.*, 2004, 2009; Wu *et al.*, 2005; Menzies *et al.*, 2007; Zheng *et al.*, 2007; Zhu *et al.*, 2012a, 2012b].

Debates on the NCC destruction have been continuing among geochemists since the beginning of the proposal of this issue decades ago [e.g., Fan and Menzies, 1992; Griffin *et al.*, 1992, 1998]. Contentions mostly focus on why, when, where, and how the destruction was processed. Timing of the onset of the destruction is a key for the understanding of the process and mechanism and bear significance for the evolution of the eastern Asian Continent. However, this has been controversial for long with varieties of estimates, that is, the Late Triassic [Han *et al.*, 2004; Yang *et al.*, 2010], Late Jurassic [Gao *et al.*, 2004], Late Cretaceous [Wu *et al.*, 2005; Yang *et al.*, 2008], and Late Carboniferous to early Cenozoic [Xu *et al.*, 2009; Windley *et al.*, 2010]. A newly detailed study argues that the destruction peaked in the Early Cretaceous [Zhu *et al.*, 2012b].

More studies are needed. One problem that needs to be answered is whether the NCC was destructed alone [e.g., Gao *et al.*, 2002; Zhang *et al.*, 2003] or together with the YTC in southern China [e.g., Wu *et al.*, 2005; Xu, 2007; Xu *et al.*, 2007; Zheng *et al.*, 2007] (Figure 1). Seismic velocity data show that the crust of the middle and east YTC is as abnormally thin (~ 30 – 33 km) [e.g., Chen *et al.*, 2008a, 2008b] as that of the NCC [Ai and Zheng, 2003] implying that the lithosphere was also thinned. Did the NCC and YTC suffer a uniform dynamic process during the Mesozoic or did they go through different processes separately?

One notable phenomenon is the voluminous felsic intrusions in the NCC and YTC [e.g., Wu *et al.*, 2005, 2011]. These rocks were overprinted by cooling related to either pure conduction or denudation. Especially, the argon system of the slowly cooled K-feldspar is sensitive to denudation owing to its nature of temperature-dependant

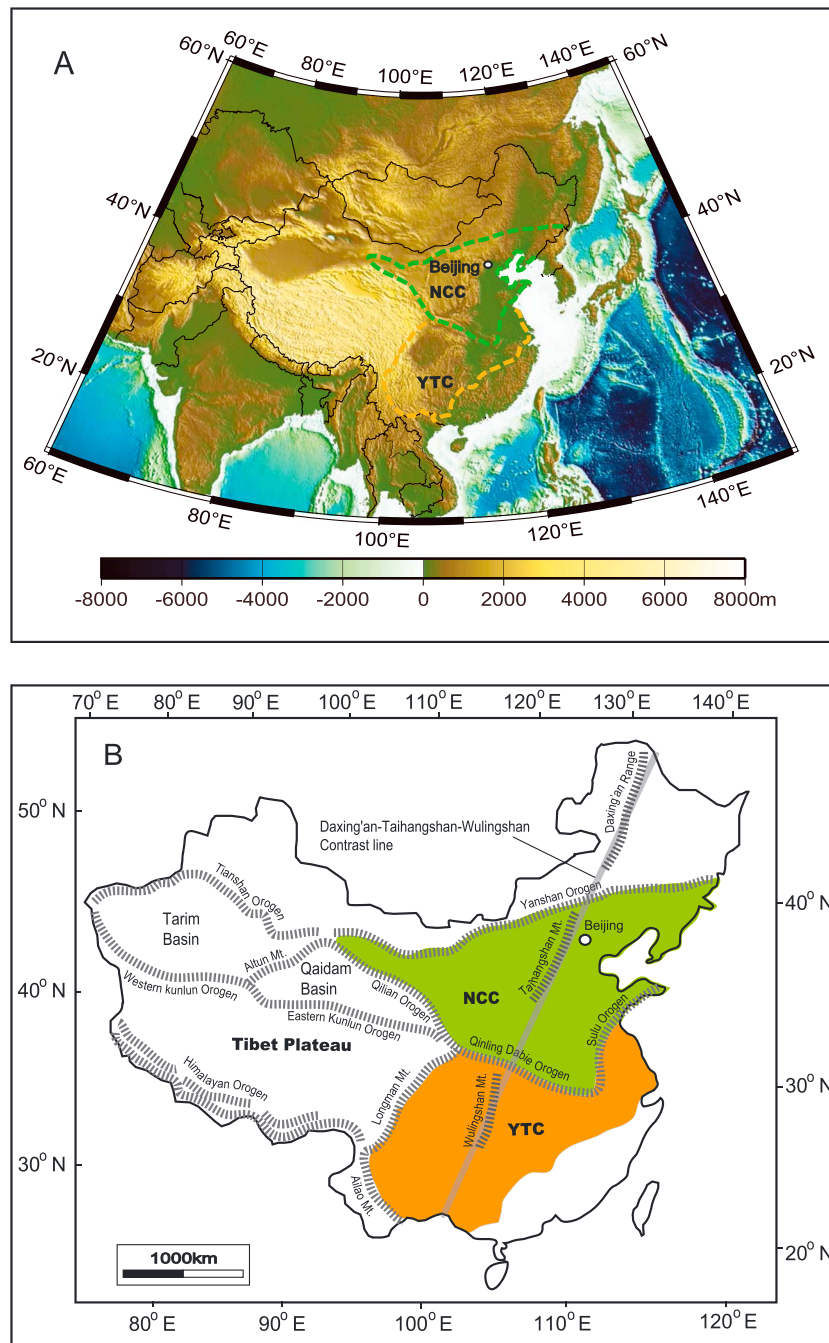


Figure 1. (a) Topography map of the East Asia (data source: *Chen, [2010]*). The North China Craton (NCC) and the Yangtze Craton (YTC) are confined by using green and orange dashed lines, respectively. (b) Schematic tectonic map of China showing the major blocks and orogens [*Wang et al., 2007*]. The North China and Yangtze Cratons are shown in green and orange, respectively. Also shown is the Daxing'an-Taihangshan-Wulingshan relief contrast line (thickest blackish solid line).

diffusion. Therefore, the slowly cooled K-feldspar can be used as a better proxy in revealing the cooling history of the rock [e.g., *Lovera et al., 1989, 1991; McDougall and Harrison, 1999*].

In this article, we study the cooling and unroofing of the NCC and YTC during the Mesozoic by using $^{40}\text{Ar}/^{39}\text{Ar}$ thermochronology and focus on the following questions: (1) Did the NCC ever experience a rapid cooling and unroofing event during the Mesozoic? If so, when and how? (2) Did the YTC thin together with the NCC? Answering these questions will shed new light on when and how the lithosphere was destructed.

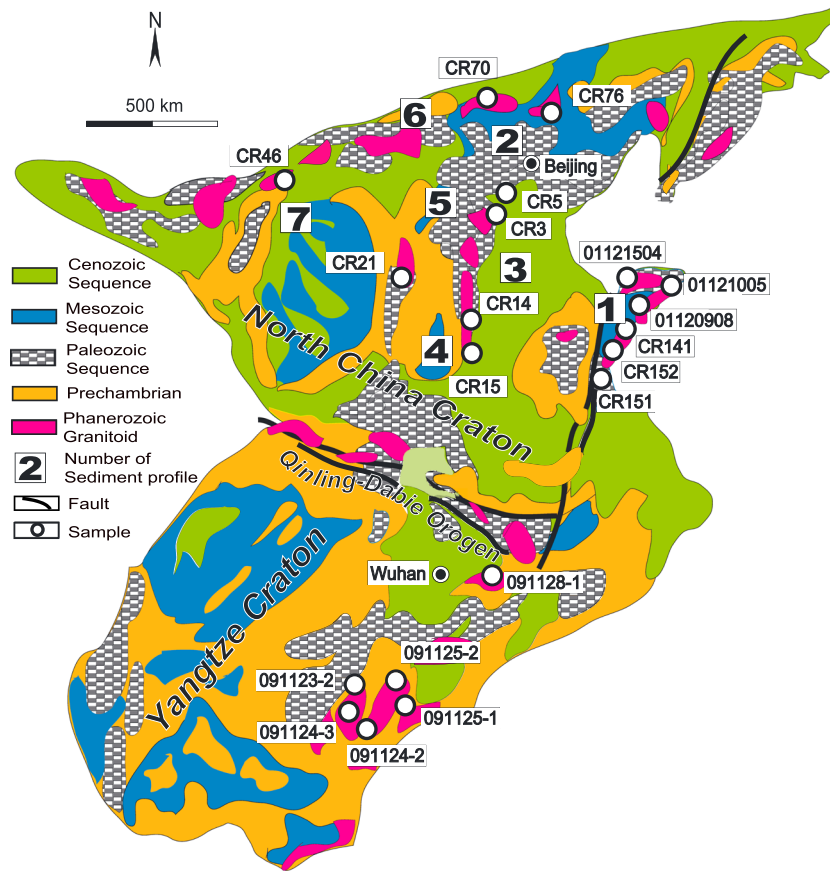


Figure 2. Geological units of North China and Yangtze Cratons (data sources are from Ma [2002] and our observations). Also shown are the sample sites and the number of sediment profiles (also see Figure 10).

2. Geological Setting

Separated by the Qinling-Dabie Orogen, the NCC and YTC are located on the north and south China, respectively (Figure 1b).

The NCC, initialized during the late Archean (2.5–3.0 Ga) [Zhai, 2011], is circumvented by the central Asian orogen (Yinshan orogen) to the north, the paleotethys belt (Qinling-Dabie orogen) to the south, the Indian-Eurasian tectonic domain (Tibet plateau) to the west, and the Sulu Orogen to the east (Figure 1b). Collision between the NCC and YTC resulted in the final closure of the Tethys Ocean and formed the Qinling-Dabie orogen during the Early Triassic [e.g., Wang et al., 2013c]. To the north, the Yinshan orogeny ceased by the Early Jurassic [Wang et al., 2013b]. The Sulu Orogen limits the NCC in the east, and the last major metamorphic event along this ultrahigh-pressure metamorphic belt occurred during 130–120 Ma [Zhang et al., 2007; Liu et al., 2008].

It has been noticed that the eastern NCC reactivated from the Paleozoic to the Early Jurassic [Gao et al., 2002; Zheng et al., 2007]. Pioneering petrological and geochemical researches have illustrated that the lithospheric mantle beneath the NCC had been removed and replaced with a thin depleted mantle domain during the Paleozoic that is associated with intensive magmatism, deformation, mineralization, and basin development [e.g., Fan and Menzies, 1992; Griffin et al., 1992, 1998]. That is, the NCC was unstable tectonically and no longer a “craton” since the Paleozoic. Studies on mantle xenoliths from Mengyin in Shandong and Fuxian in Liaoning captured by diamond-bearing kimberlite at ~470 Ma suggested a ~200 km thick lithosphere at that time [Fan and Menzies, 1992; Griffin et al., 1992, 1998], whereas xenoliths from Cenozoic basalts indicate that the thickness of the lithosphere was thinned to 80–120 km [Chi and Lu, 1992; Fan and Hooper, 1989]. Hence, the lithosphere of the NCC must have lost a portion of ~120 km thickness, probably in the Mesozoic. Geophysical observations indicate that the present-day NCC lithosphere is ~70 km thick [e.g., Chen et al., 2008a, 2008b], affirming that it has been greatly destructed and thinned.

Table 1. Summary of the Sample Location, Mineralogy, ⁴⁰Ar/³⁹Ar Ages, and Emplacement Ages^a

Sample	Pluton	Rock Type	Location	Mineralogy	⁴⁰ Ar/ ³⁹ Ar Age (Ma)		Emplacement Age (Ma) (Zircon U/Pb Age)	ΔT (Myr)
					Kf Maximum Age at 1100°C	Bio Plateau Age		
CR3	—	Deformed diorite	N39°24.475' E115°10.683'	Mylonitic texture, eye-shaped feldspar, and quartz. Fine-grained foliated biotite.	302.5 ± 2.0 324.8 ± 1.9 134.0 ± 1.6	—	—	
CR5	Wang'an	Granite	N39°28.068' E115°09.927'	Coarse-grained biotite, quartz, and K-feldspar. Zircon, sphene, and other oxides.	125.7 ± 1.8 121.4 ± 0.8 99.5 ± 1.6	142.5 ± 1.8, Wang and Li [2008]	21.1	
CR14	Hongshan	Syenite	N36°45.070' E114°24.654'	K-feldspar > 90% quartz, and amphibole. Sphene, zircon, and other oxides.	— 122.0 ± 1.0 100.7 ± 6.6	132 ± 2, Chen et al. [2008a, 2008b]	10.0	
CR15	Xishu	Diorite monzonite	N36°38.294' E114°00.536'	Coarse-grained quartz, K-feldspar, and plagioclase. Sphene, zircon, and other oxides	— 223.3 ± 4.6 107.6 ± 10.7	241.0 ± 2.8, Ying et al. [2011]	17.7	
CR21	Huyuanshan	Granitic syenite	N37°43.263' E111°55.316'	Coarse-grained K-feldspar, quartz, zoned plagioclase, and biotite.	— 122.6 ± 5.9 94.6 ± 9.8	129.9 ± 2.3, Ying et al. [2011]	7.3	
CR46	Langshan	Quartz diorite	N41°10.540' E107°08.605'	Zircon, sphene, and other oxides. Coarse-grained quartz, K-feldspar, plagioclase, and amphibole.	— 160.0 ± 1.0 49.0 ± 2.1	—	—	
CR70	Kulongshanbei	Adamellite	N41°30.149' E116°43.879'	Sphene, zircon, and other oxides. Coarse-grained plagioclase, K-feldspar, quartz, and biotite. Zircon, sphene, and other oxides	— 135.6 ± 1.6 73.9 ± 6.8	~137, Zhu and Yang [1998]	1.4	
CR76	Changshanling	Granite	N40°46.222' E117°26.201'	Rapakivi texture, zoned k-feldspar, plagioclase, quartz, amphibole, biotite. Zircon, sphene and other oxides	— 166.2 ± 1.8 129.4 ± 3.6	191.7 ± 2.3, BGM/RNM, 1991	25.5	
CR141	—	Felsic mylonite	N35°58.194' E119°58.828'	Mylonitic texture, elongated feldspar and quartz. Fine-grained foliated biotite	— 130.4 ± 0.8 104.7 ± 0.9	—	—	
CR151	Wulian	Monzodiorite	N35°39.785' E119°22.587'	Coarse-grained K-feldspar, quartz and biotite. Zircon, sphene and other oxides	— 119.9 ± 0.9 106.9 ± 3.7	122 ± 2, Yang et al., 2005	2.1	
CR152	—	Felsic mylonite	N35°30.836' E119°16.132'	Mylonitic texture, elongated feldspar and quartz.	— 143.7 ± 1.2 78.4 ± 4.2	—	—	
01121005	—	Granitic gneiss	Shidao shear-zone, Daoxitou, Shandong	Fine-grained foliated biotite. Foliated K-feldspar, quartz, silicic plagioclase, biotite.	— 128.5 ± 0.7 102.9 ± 0.6	—	—	
01120908	—	Dioritic gneiss	Rongcheng nappe, Dashijia, Shandong	Zoned garnet, kyanite, sillimanite. Foliated K-feldspar, quartz, amphibole, plagioclase. Garnet, kyanite, sillimanite	— 203.0 ± 1.0 124.1 ± 0.7	—	—	

Table 1. (continued)

Sample	Pluton	Rock Type	Location	Mineralogy	⁴⁰ Ar/ ³⁹ Ar Age (Ma)			ΔT (Myr)
					Kf Minimum Age	Bio Plateau Age	Emplacement Age (Ma) (Zircon U/Pb Age)	
01121504	—	Granitic mylonite	Muping shear-zone, Wanggezhuang, Shandong	Mylonitic texture, eye-shaped feldspar, quartz. Fine-grained foliated biotite	—	—	—	—
091123-2	Taojiang	Granite	N28°30.436' E112°03.614'	Coarse-grained biotite, quartz and K-feldspar. Zircon, sphene and other oxides	209.6 ± 1.4	220 ± 2	220 ± 2	23.7
091124-2	Weishan	Adamellite	N27°51.990' E112°13.613'	Coarse-grained K-feldspar, slightly sericitic zoned plagioclase, biotite, quartz. Sphene, zircon and other oxides	199.8 ± 2.6	222 ± 3	222 ± 3	19.0
091124-3	Weishan	Adamellite	N28°00.060' E112°00.849'	Paragenesis similar to the 091124-2	203.0 ± 1.2	222 ± 3	222 ± 3	23.2
091125-1	Ziyunshan	Biotite granite	N27°27.872' E112°21.267'	Coarse-grained biotite, quartz and K-feldspar. Zircon, sphene and other oxides	201.5 ± 2.2	—	—	—
091125-2	Gaoping	Adamellite	N27°33.730' E112°26.773'	Coarse-grained K-feldspar, plagioclase, quartz, biotite. Zircon, sphene and other oxides	198.8 ± 1.2	—	—	—
091128-1	Huangshi	Biotite granite	N30°00.660' E115°00.187'	Coarse-grained biotite, quartz and K-feldspar. Zircon, sphene and other oxides	55.4 ± 2.3	—	—	—
					174.9 ± 2.9	—	—	—
					164.2 ± 1.0	—	—	—
					69.0 ± 1.1	—	—	—
					151.4 ± 3.6	—	—	—
					170.8 ± 1.0	—	—	—
					53.2 ± 3.1	—	—	—
					127.3 ± 1.4	—	—	—
					131.0 ± 0.8	—	—	—
					76.2 ± 3.1	—	—	—

^aErrors are at 2σ level. Note that ΔT is the difference between maximum age of K-feldspar and emplacement ages.

The YTC is relatively younger than the NCC. It has a Paleoproterozoic to Mesoproterozoic basement overlain by a Neoproterozoic (Sinian) to Cenozoic cover [Xu *et al.*, 2007]. Although the crusts of the NCC and YTC have distinct ages and evolution histories, their lithospheres are quite comparable in terms of lithology, geochemistry, and mineralogical composition [Fan and Hooper, 1989; Xu *et al.*, 2007]. The present-day thin lithosphere of the YTC implies that it was also thinned at sometime.

There is a significant topographic contrast in East Asia, comprising high plateaus in the west and low plains in the east, separated by the Daxing'an-Taihangshan-Wulingshan belt (Figure 1b). This contrast lineation coincides with the steepest gradient in gravity anomalies and crustal thickness [Chen *et al.*, 2008a, 2008b]. Interestingly, it also marks the steepest gradient in the mantle's seismic velocity clearly seen at depths of 100 km and 150 km [Chen *et al.*, 2008a, 2008b].

3. Samples, ⁴⁰Ar/³⁹Ar Geochronology, and Results

Samples collected from the NCC and YTC, and K-feldspars were carefully checked to match the criteria or requirements for thermochronological study [Lovera *et al.*, 1997, 2002]. For example, the K-feldspar that partially altered to adularia, and/or replaced all earlier microtextures with ultraporous late feldspar was eliminated by using electronic microscope probe analyses. These K-feldspars had undergone recrystallization at temperatures of <450°C [Parsons *et al.*, 2013], making them unsuitable for thermochronological study [Lovera *et al.*, 1997, 2002] (see discussion later).

Twenty samples of Mesozoic age or older were selected and subjected to high-resolution ⁴⁰Ar/³⁹Ar geochronological and thermochronological studies. They were collected from major Mesozoic intrusive bodies at as many localities to observe whether and when the vast area ever underwent a uniform cooling history (Figure 2). These samples are lithologically the undeformed granitoids, granitic gneisses, and mylonites (Table 1). Except CR3, all the others were previously dated as Mesozoic products [e.g., Bureau of Geology and Mineral Resources of Nei Mongolia Autonomous Region (BGMRNM), 1991; Yang *et al.*, 2005; Zhang *et al.*, 2007, 2010; Chen *et al.*, 2008a, 2008b; Liu *et al.*, 2008; Wang and Li, 2008; Ying *et al.*, 2011; Zhao *et al.*, 2011; Chu *et al.*, 2012a, 2012b; Wang *et al.*, 2013b, 2013c]. CR3 is from an Archean diorite in the northern part of the NCC, which was strongly deformed in the Late Paleozoic [BGMRNM, 1991; Wang and Li, 2008].

To reveal the argon distribution within the K-feldspar grain as finely as possible, the high-resolution (36–40 steps) step-heating technique of ⁴⁰Ar/³⁹Ar analysis was used. Biotites (when available) were also analyzed to compare with the K-feldspars. The experiments were conducted in the Institute

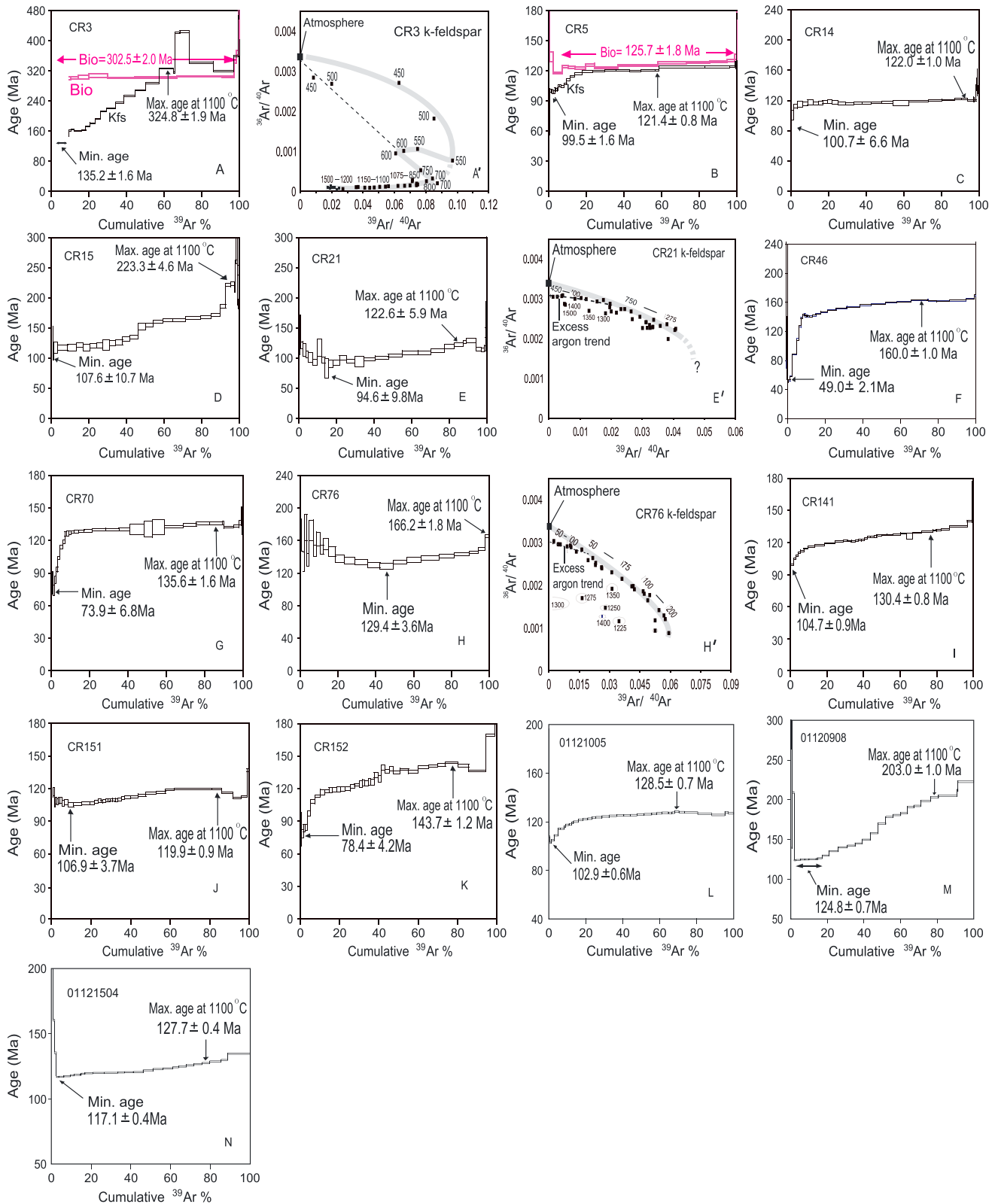


Figure 3. (a–n) Age spectra of the K-feldspars (in black) and two biotites (in red) from the NCC. Minimum and maximum ages of the K-feldspar are labeled. Minimum age refers to the age from which the age spectrum ascends monotonically. Maximum age is the highest age at 1100°C, over which the K-feldspar frame will collapse. The inverse isochrons of CR3, CR21, and CR76 are also shown. See text for details.

of Geology and Geophysics of the Chinese Academy of Sciences. The sample processing and $^{40}\text{Ar}/^{39}\text{Ar}$ analysis procedures are shown in Appendix S1 in the supporting information.

Detailed $^{40}\text{Ar}/^{39}\text{Ar}$ analytical results of the 20 K-feldspars and eight biotites are listed in Appendix S2 and are summarized in Table 1 together with the sampling locations, mineralogy, and emplacement ages (zircon U/Pb age) of some undeformed plutons taken from the literature. Age spectra are shown in Figures 3 and 4. Maximum and minimum ages of the K-feldspar and the plateau ages of the biotite are presented in Table 1 and Figures 3 and 4, respectively. The minimum age refers to the age from which the age ascends monotonically and the maximum age is the highest age before the crystalline frame of K-feldspar collapses during in vacuo heating over 1100°C [Lovera *et al.*, 1989; McDougall and Harrison, 1999]; however, in some cases (where no high-temperature excess argon is present), an integral age of steps degassed above 1100°C would also provide a good estimate of the maximum closure age. The collapsing of the crystalline frame destroys the age structure recorded by the K-feldspar [Lovera *et al.*, 1989].

All K-feldspars from the NCC exhibit staircase-shaped age spectra (Figure 3). Inverse isochron plot of CR3 (Figure 3a' and Appendix S2) shows a curve characterized by a monotonically rising age spectrum. The curve extends to atmospheric argon composition suggesting that the age gradient is not related to excess argon. The steps at low temperatures (450 and 500°C, Figure 3a' and Appendix S2) appear to be because of excess argon but cannot affect anything because of the very small percentage (<0.1%) of total released argon (Appendix S2). The steps between 550 and 700°C deviate from the curve and form a straight line extending to the atmospheric argon composition and yielding an isochron not related to excess argon.

CR21 and CR76 exhibit a descending pattern at low-temperature steps accounting for ~17% and 45% of the total released argon, respectively (Figures 3e and 3h) suggesting excess argon affiliated as indicated by the inverse isochron diagrams (Figures 3e' and 3h'). The steps at temperatures between 450 and 800°C (Figure 3e' and Appendix S2) and 450 and 750°C (Figure 3h' and Appendix S2) of CR21 and CR76 extend (dashed line) to the initial argon compositions of the excess argon, respectively. The high-temperature steps for both samples form a gentle curve extending to the atmospheric argon composition (Figures 3e' and 3h') suggesting that no excess argon contained in these steps. The last eight steps (1150–1400°C) of CR76 show a trend toward excess argon component (Figure 3h'), but they do not affect the entire age spectrum because of the very small percentage of released argon (<0.5%, Figure 3h and Appendix S2). Abnormal ages also occur at the very first steps of 01120908 and 01121504 (Figures 3m and 3n) accounting for <2% of the total argon, implying the presence of excess argon from the alteration at the very surface of the minerals that can be degassed at very low temperatures (450–550°C).

Almost all the feldspars from the YTC illustrate perfect monotonic staircase-shaped age spectra (Figure 4) except 091128–1 that yields a flat age plateau (accounting for 85% of the released argon) at high temperatures (Figure 4f). The isochron plot of 091123–2 shows a curve extending to the initial argon composition of atmosphere suggesting that there is no excess argon residing in the sample (Figure 4a').

Eight biotites yield flat age spectra with well-defined plateau ages close to the maximum ages of the K-feldspars (Table 1, Figures 3, and 4). This suggests that the usual perthitization of the K-feldspar did not affect the argon diffusion apparently [Mock *et al.*, 1999] although possible flaws might rise from the perthitization and complex microtexture in the K-feldspars [Parsons *et al.*, 1991; Villa, 1994]. This will be discussed later.

4. $^{40}\text{Ar}/^{39}\text{Ar}$ Geochronological Results

4.1. The NCC

A wide age range of K-feldspar with maximum ages ranging from 324.8 to 119.9 Ma is exhibited in Table 1 and Figure 3. These ages reflect consistent information on timing sequence with zircon U/Pb ages in the same parental rock, respectively, from the previous studies [e.g., BGMRNM, 1991; Yang *et al.*, 2005; Zhang *et al.*, 2007, 2010; Wang and Li, 2008; Chen *et al.*, 2008a, 2008b; Ying *et al.*, 2011; Zhao *et al.*, 2011; Wang *et al.*, 2013b].

The last major metamorphic event along the Sulu ultrahigh-pressure metamorphic belt occurred during 130–120 Ma [Zhang *et al.*, 2007; Liu *et al.*, 2008], which is consistent with the K-feldspar maximum ages identified in this study (130.4 ± 0.8 Ma for CR141, 128.5 ± 0.7 Ma for 01121005, and 127.4 ± 0.4 Ma for 01121504). This event can also be identified from the age spectrum of the Paleozoic gneissic sample of 01120908. The relative flat portion accounting for ~20% of the total released argon around ~124 Ma suggests a rapid cooling event at this time (Figure 3m). The age spectrum of the mylonitic sample CR152 shows a relative flat portion of ~30% of

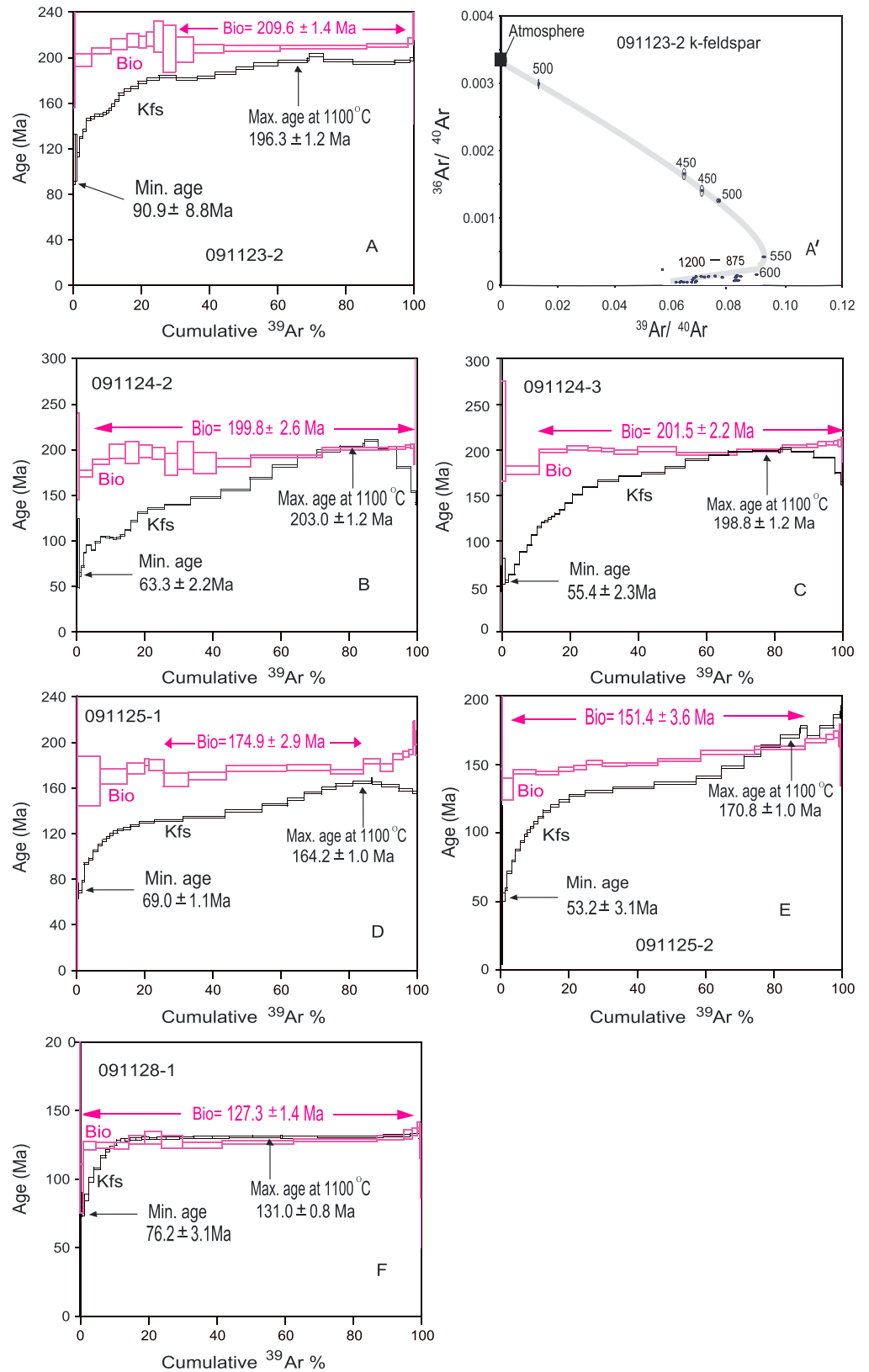


Figure 4. (a–f) Age spectra of the K-feldspars and biotites from the YTC. Minimum and maximum ages of the K-feldspar are labeled. Minimum age refers to the age from which the age spectrum ascends monotonically. Maximum age is the highest age at 1100°C, over which the K-feldspar frame will collapse. The inverse isochron of 091123–2 are also shown.

the released argon around 120 Ma suggesting that final rapid cooling event recorded occurred at this time followed by a very slow cooling period until 78.4 Ma (Appendix S2 and Figure 3k). Granitoids intruded the Sulu belt in a range from 130 to 120 Ma indicated by zircon U/Pb ages [e.g., Yang *et al.*, 2005; Zhang *et al.*, 2010; Zhao *et al.*, 2011], consistent with the K-feldspar maximum age (119.9 ± 0.9 Ma) of the granite sample CR151 (Figure 3j).

An Archean diorite (1745 Ma) [Wang and Li, 2008] that outcropped in the Taihang range in the middle of NCC was overprinted by two metamorphic events [Wang and Li, 2008]. A Late Paleozoic event (~ 358 Ma) [Wang and Li, 2008] may have reset the diorite, which is reflected by the maximum K-feldspar age (324.8 ± 1.9 Ma) and biotite age (302.5 ± 2.0 Ma) of CR3 (Figure 3a). A rapid exhumation event during 142–120 Ma then followed [Wang and Li, 2008], which is reflected by a relatively flat portion ($\sim 9\%$ of released argon) around 135 Ma in the age spectrum of the K-feldspar of CR3 (Figure 3a). Cretaceous undeformed granitoids along the Taihang range emplaced at ~ 132 Ma (zircon U/Pb age) [Chen *et al.*, 2008a, 2008b] are 7–10 Myr older than the maximum ages of the K-feldspars and biotite in this study (maximum K-feldspar age 121.4 ± 0.8 Ma and biotite age 125.7 ± 1.8 Ma for CR5 and maximum K-feldspar age 122.0 ± 1.0 Ma for CR14). The zircon U/Pb age of the Middle Triassic granite in the Taihang range is around 241 Ma [Ying *et al.*, 2011], ~ 18 Myr older than the maximum K-feldspar age of CR15 (223.3 ± 4.6 Ma).

Despite the variation of the maximum ages, the minimum ages of K-feldspars are relatively more uniform (99.5 ± 1.6 Ma for CR5, 100.7 ± 6.6 Ma for CR14, and 107.6 ± 10.7 for CR15) if 2 sigma errors are considered. For example, the maximum and minimum ages of K-feldspar of the undeformed syenite CR21 from the Lvliang range, 122.6 ± 5.9 and 94.6 ± 9.8 Ma, respectively, are similar to the undeformed granitoids in the nearby Taihang range, suggesting that both ranges had experienced a similar cooling history.

Samples CR46, CR70, and CR76 were collected along the Yinshan range, the northern margin of NCC (Figure 2). CR46 and CR76 intruded in the Early Jurassic [BGMRNM, 1991] and the maximum ages of their K-feldspars are 160 ± 1.0 and 166.2 ± 1.8 Ma (Figures 3f and 3h), respectively. The maximum age of CR70 is 135.6 ± 1.6 Ma, which corresponds with the early Yanshanian emplacement event (~ 137 Ma) [Zhu and Yang, 1998].

4.2. The YTC

Five of the six undeformed granitoid samples from the YTC (091123–2, 091124–2, 091124–3, 091125–1, and 091125–2) were collected from the Xuefengshan range (Figure 2) in the middle eastern part of YTC. They yielded maximum ages from 164.2 to 203.0 Ma and minimum ages from 53.2 to 90.9 Ma (Figures 4a–4e). The Xuefengshan range is an Early Triassic orogen but it has experienced the Late Triassic to Early Jurassic postorogenic magmatism after folding and synmetamorphic ductile deformation [Chu *et al.*, 2012a, 2012b; Wang *et al.*, 2013c]. The emplacement of the Early Mesozoic plutons is well constrained ranging from 225 to 215 Ma in a recent study [Chu *et al.*, 2012a, 2012b]. Sample 091128–1 presents a very distinct age spectrum pattern and a much younger maximum age (131.0 Ma) than the other five, suggesting that it has experienced a distinct cooling history. Its biotite age is similar to those of the postcollisional undeformed granites in the Dabie ultrahigh metamorphic belt (Zircon U-Pb and biotite $^{40}\text{Ar}/^{39}\text{Ar}$ ages of 110–130 Ma) [Zhao *et al.*, 2011; Wang *et al.*, 2013a]. The pattern of the K-feldspar age spectrum (Figure 4f) is also similar to those observed on the Dabie granites [Wang *et al.*, 2013a]. In addition, the nearby location (Figure 2) also emphasizes a close relationship of the magmatic genesis between 091128–1 and those undeformed granites of the Late Mesozoic in Dabie.

4.3. Pure Conductive (In Situ) Cooling and Its Implications

Discrepancy between emplacement age (zircon U/Pb age) and $^{40}\text{Ar}/^{39}\text{Ar}$ K-feldspar minimum age from a same rock is a result of cooling [Dodson, 1973] from ~ 900 to 150°C . This is inferred based on the well-accepted assumptions of closure temperature of (T_c) 900°C for zircon U-Pb system [e.g., Cherniak and Watson, 2000] and ~ 450 (or 400)– 150 (or 200) $^\circ\text{C}$ for K-feldspar argon system [e.g., Lovera *et al.*, 1989, 1991; Warnock and Zeitler, 1998; Cassata and Renne, 2013]. Owing to the lower temperature in the surrounding environment than in the emplaced rock in the middle to upper crust (30–10 km, a usual emplacement depth of granitoids), the cooling from ~ 900 to $\sim 500^\circ\text{C}$ normally reflects a pure conductive (in situ) cooling. In contrast, cooling from $\sim 500^\circ\text{C}$ down to the ground surface temperature is usually related to the unroofing and denudation process [Mock *et al.*, 1999; McDougall and Harrison, 1999].

An interesting phenomenon that should be noticed is the variation of pure conductive cooling rate exhibited by the undeformed granitoids from the NCC and YTC. Table 1 shows that the samples with emplacement

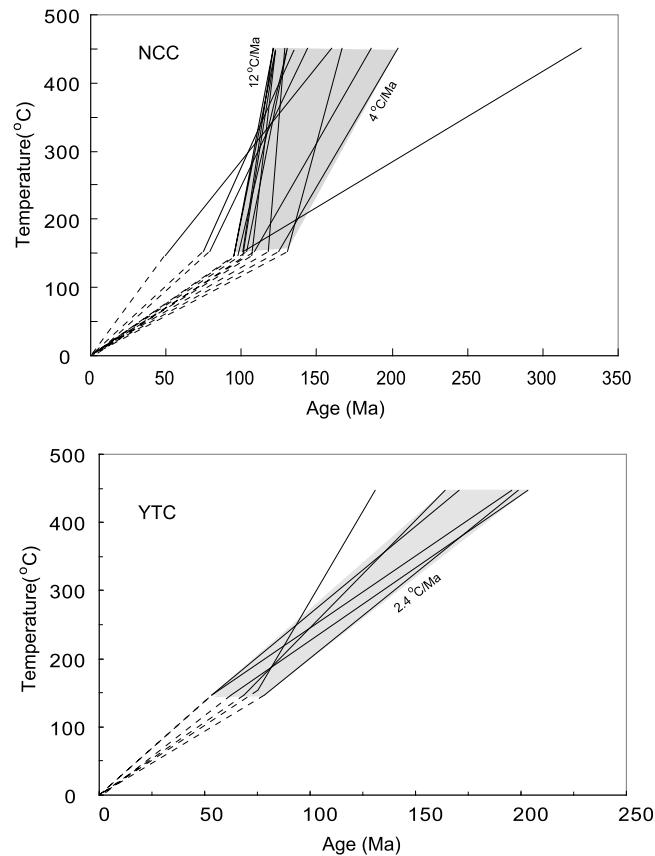


Figure 5. Average cooling histories for the upper crusts of the NCC and YTC by connecting the maximum and minimum ages of the K-feldspar via the temperatures that they reflect. A rapid cooling ($12^{\circ}\text{C}/\text{Ma}$) event is discovered during the Early Cretaceous in the NCC that reflects unroofing. In contrast, the cooling of the YTC was much gentler ($2.4^{\circ}\text{C}/\text{Ma}$), showing that no rapid unroofing event occurred during 200–75 Ma. See text for details.

slow pure conductive cooling rate. Again, this might mean that the YTC crust in the Late Triassic to Late Jurassic was thicker than the NCC in the Cretaceous.

The absolute intrusive depth of a granitoid can be estimated by using the initial flat portion (when available) of the cooling history recovered from K-feldspar and geothermal gradient (see section 5). A granitoid emplaced in the middle to upper crust would cool until it “nearly” equilibrates with the ambient temperature of the surrounding environment which strongly depends on the emplacement depth. That is, the granitoid “stayed” at its emplacement place until was unroofed. Thus, the initial flat portion of the cooling history reflects the “stay” before unroofing and denudation event. The samples CR3 and CR15 are characterized by a manifest flat portion at $\sim 300^{\circ}\text{C}$ during ~ 300 – 150 Ma and ~ 200 – 140 Ma (section 5 and Figure 8), giving an estimate of emplacement depth of 15 km assuming a geothermal gradient of $\sim 20^{\circ}\text{C}/\text{km}$ during Triassic and Jurassic in the central and eastern NCC [Zhai *et al.*, 2004]. The flat portion of CR21 (Figure 8) at $\sim 300^{\circ}\text{C}$ during ~ 150 – 120 Ma (section 5 and Figure 8) implies an emplacement depth of 8.8 km (geothermal gradient $\sim 34^{\circ}\text{C}/\text{km}$ in Late Jurassic and Cretaceous) [Zhai *et al.*, 2004]. These estimates are quite consistent with the conclusions obtained by using the “pure cooling” rate.

4.4. Average Cooling Rates of the NCC and YTC

Argon distribution in the K-feldspar is a result of cooling from ~ 450 (or 400)– 150 (or 200) $^{\circ}\text{C}$ [e.g., Lovera *et al.*, 1989, 1991; Warnock and Zeitler, 1998; Cassata and Renne, 2013]. The cooling at these temperatures is usually related to unroofing and denudation [Lovera *et al.*, 1989; McDougall and Harrison, 1999]. The average cooling history from ~ 450 to 150°C can be directly estimated by the K-feldspar maximum and minimum ages via their corresponding T_c in the T - t plot (Figure 5). Figure 5 shows two distinct cooling patterns on the NCC and YTC.

ages ranging from 130 to 120 Ma have a shorter duration (<10 Myr, Table 1) between their emplacement ages and K-feldspar maximum ages than those emplaced before 140 Ma (~ 18 – 25 Myr, Table 1). This suggests that the Cretaceous granitoids in the NCC had faster pure conductive cooling rates than the Jurassic ones. There are two possibilities for this: (1) the thermal gradient in the Cretaceous was lower than in the Jurassic, and (2) the rocks intruded higher into the crust in the Cretaceous than in the Jurassic. In the central and eastern NCC, the geothermal gradient was lower in Triassic ($\sim 20^{\circ}\text{C}/\text{km}$) [Zhai *et al.*, 2004] than in Cretaceous ($\sim 34^{\circ}\text{C}/\text{km}$) [Zhai *et al.*, 2004]; and it was constant in Late Jurassic, Cretaceous, and Cenozoic ($\sim 35^{\circ}\text{C}/\text{km}$) [Wang *et al.*, 1985; Zhai *et al.*, 2004]. Therefore, the first possibility is excluded, and the rocks intruding high during the Cretaceous is the reason for the rapid in situ cooling rate. Petrologically, there is no mechanism for the magma to be emplaced high widely unless the crust is thin. Therefore, we conclude that there was a thinner crust in the Cretaceous than in the Jurassic for the NCC.

Similarly, samples from the YTC (091123–2, 091124–2, and 091124–3) also exhibit a big discrepancy (~ 19 – 23.7 Myr, Table 1) between the K-feldspar maximum ages and emplacement ages suggesting a

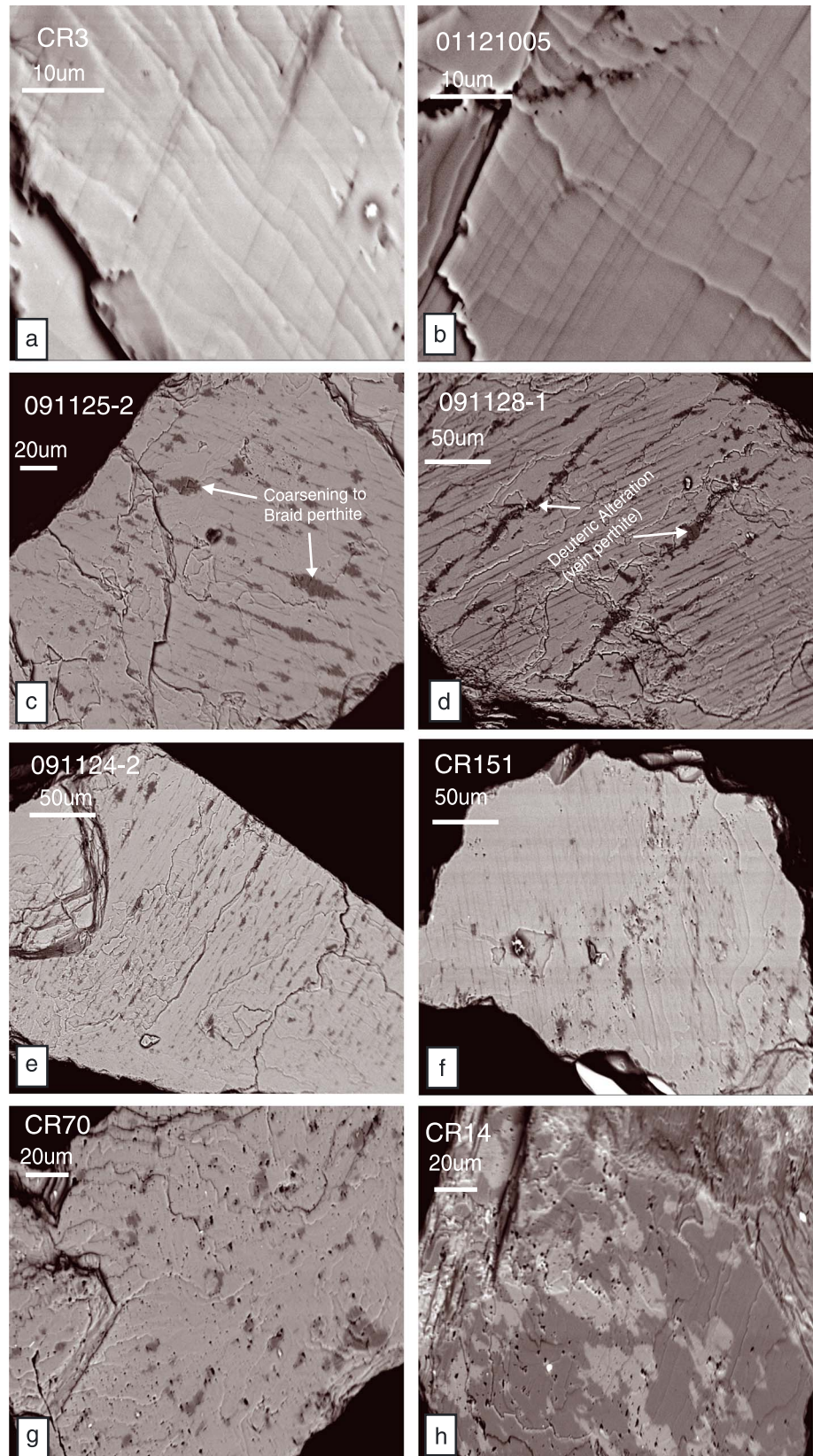


Figure 6

The upper crust of the NCC cooled more rapidly than that of the YTC during the Late Mesozoic. Despite the dispersion, half of the samples from the NCC show similar patterns that cooled from ~450 to 150°C in a relatively short range from ~140 to ~95 Ma (Figure 5), yielding a cooling rate of 12°C/Ma. In contrast, all the samples from the YTC cooled from ~450 to 150°C in the range from ~180 to ~75 Ma, giving a cooling rate of 2.4°C/Ma (Figure 5).

Therefore, the estimation of average cooling histories suggests that the upper crusts of the NCC and YTC experienced different cooling processes during the Late Mesozoic. To understand the details, quantitative modeling of geothermal histories for the NCC and YTC is needed.

5. Thermochronological Modeling

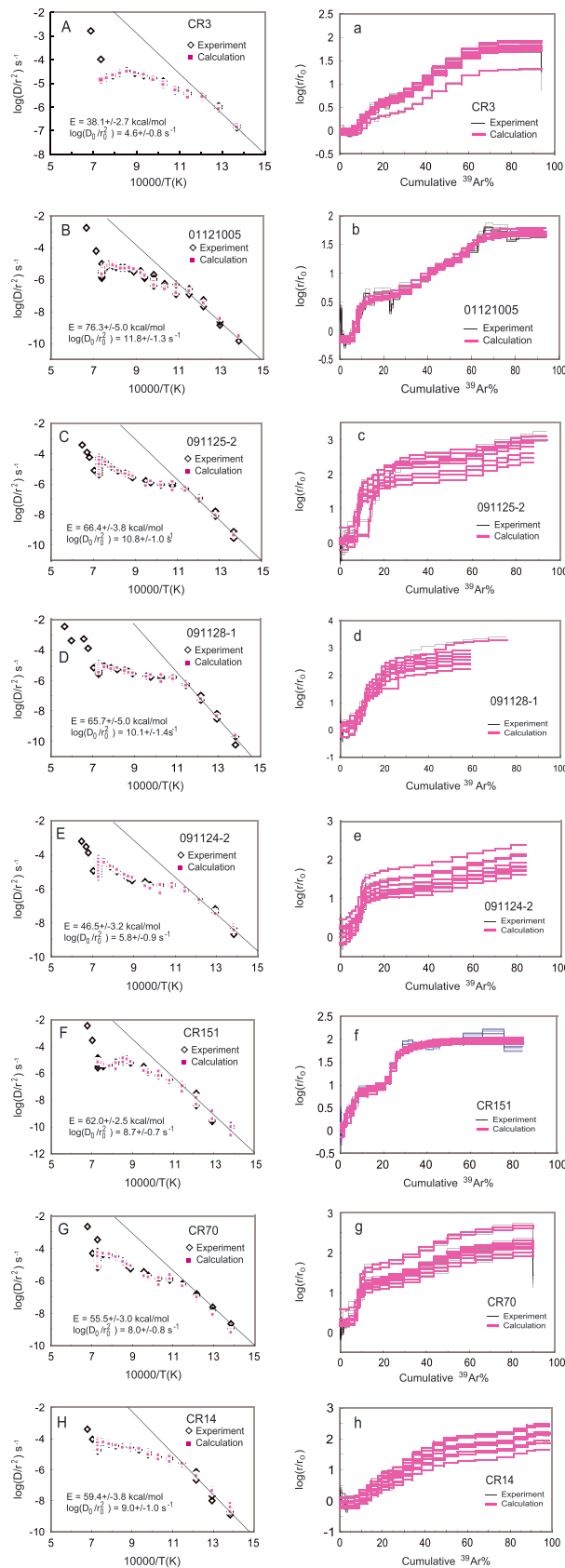
Average cooling histories imply that the upper crust of the NCC cooled more rapidly than that of the YTC during the Late Mesozoic. This stimulates us to determine the nonlinear cooling pattern, which may be hidden in the argon distribution within the K-feldspar. Slowly cooled K-feldspars display complex and variable microstructures and as a result, potentially record $^{40}\text{Ar}/^{39}\text{Ar}$ ages over a range of temperatures spanning 250°C as they cool [Wartho *et al.*, 1999]. Thus, K-feldspar represents an important resource for understanding thermal histories. Based on argon released by the stepped heating, a series of models were proposed to explain the range of ages and more importantly, to infer thermal histories. The models have reached a high level of sophistication, yet there is no general agreement over the relationship between argon diffusion and observable microtextures [e.g., Lovera *et al.*, 1991; Lee, 1995; Arnaud and Kelley, 1997; Wartho *et al.*, 1999; Parsons *et al.*, 1999; Reddy *et al.*, 1999, 2001; Cassata and Renne, 2013].

Multidomain diffusion (MDD) model [Lovera *et al.*, 1989, 1991; McDougall and Harrison, 1999] is most widely used to calculate the cooling history. Although its validity has been argued for long [Arnaud and Kelley, 1997; Parsons *et al.*, 1999; Reddy *et al.*, 1999, 2001; Wartho *et al.*, 1999], some geological observations lend substantial support to the MDD model. For instance, a sample from the bottom of the KBT (Kontinentales Tiefbohrprogramm der Bundesrepublik Deutschland) borehole [Warnock and Zeitler, 1998] at a depth of 9 km with a geothermal temperature of 265°C produced a staircase-shaped age spectrum of K-feldspar of 0–450 Ma. The minimum age of 0 Ma suggests that at least a portion (domain?) of the K-feldspar holds a closure temperature lower than 265°C, making its argon system open until the present (0 Ma).

One of the main arguments against MDD modeling is that microstructural features, particularly low-temperature alteration [Parsons *et al.*, 1999] or deformation [Reddy *et al.*, 2001], are able to affect the argon domains within a feldspar over geological time, at or below the closure temperatures of individual domains. Typical features of microstructurally complex K-feldspars include perthitic lamellae, micropores and deuterically recrystallized zones of albite, and/or micropertthite [Parsons *et al.*, 1999]. Detailed studies on argon diffusion showed that these alteration and/or incoherent subgrain intergrowths define diffusion domains [Parsons *et al.*, 1999; Cassata and Renne, 2013]. K-feldspars selected from undeformed granites whose alteration and crystallization features are characterized only by comagmatic microtextures (e.g., deuteritic turbidity, strain-controlled exsolution, and symplectically crystallized mymekite) represent suitable candidates for the MDD model [e.g., McLaren and Reddy, 2008; Cassata and Renne, 2013]. Routine examination of samples using petrographic microscope, electron microscope, or scanning electron microscope (SEM) is generally sufficient to assess the nature of diffusion domains and the suitability of a given sample for thermal modeling.

When examined under the SEM, unirradiated grains of the K-feldspars of all samples selected in this study show three types of microstructural features represented by examples in Figure 6: (1) unaltered coherent cryptoperthite and intergrowths (Figures 6a and 6b). This strain-controlled film perthite is the original microstructure of K-feldspar formed at or above 850°C during magmatism [Parsons *et al.*, 2013]; (2) coarsening to braid micropertthite and deuteritic vein perthite crosscutting and obscuring the film perthite (Figures 6c–6f), are products at or above 700°C during later magmatism [Parsons *et al.*, 2013]. Most samples in this study are characterized by this type of microstructural feature; (3) deuteritic coarsening patch perthite

Figure 6. Backscattered electron (BSE) images of representative samples illustrating perthitic microtextures of K-feldspars from the NCC and YTC. Three types of microtexture features can be identified: (a and b) unaltered coherent cryptoperthite and intergrowths, (c–f) coarsening to braid micropertthite and deuteritic vein perthite crosscutting and obscuring the film perthite, and (g and h) deuteritic coarsening patch perthite.



perthite (Figures 6g and 6h). Dissolution-precipitation reaction leads to partial replacement of braided microperthite by microporous mosaic of incoherent low albite and low microcline subgrains formed at 500°C 1000 years after magmatic emplacement [Parsons et al., 2013].

Thus, the microtextures of K-feldspars in this study all formed during initial cooling of the plutons at or above 500°C within less than 10^4 years of emplacement. These temperatures are higher than the closure temperature of K-feldspar of 350–150°C, showing that the argon distributions within these K-feldspars were not disturbed by the formation of microtexture. SEM backscattered electron (BSE) images do not reveal subgrain growth or other microstructural features that could be attributed to deformation, which conforms with the observation of no alteration minerals such as white-mica or sericite in thin sections and with undeformed features of the hand samples. Therefore, the samples in this study should be viable candidates for thermal modeling because the timing of formation and subsequent integrity of the diffusion domains can be assessed.

Arrhenius arrays (Figures 7A–7H, black solid diamond) obtained from K-feldspar crystals of the samples shown in Figure 6 are consistent with a range in diffusive length scales (multiple domains) depicted by Cassata and Renne [2013]. They are characterized by linear arrays at low-temperature portions (<700°C, Figure 7) and big curvatures at high-temperature portions (>900°C, Figure 7). The deviations from linearity on step-heating Arrhenius plots may reflect the effect of the exhaustion of subgrain domains of interesting size [Lovera et al., 1989, 1991; Cassata and Renne, 2013].

Figure 7. (A–H) Argon-39 Arrhenius plots (black diamonds) and (a–h) $\log(r/r_0)$ plots (black lines) for prograde heating of samples in Figure 6, calculated using equations for slab diffusion geometry. Arrhenius plots (red squares in Figures 7A–7H) and $\log(r/r_0)$ plots (red lines in Figures 7a–7h) of automated MDD modeling for the same sample fit well with the experimental results. Uncertainties in D/a^2 values are generally smaller than the symbols, but are not shown.

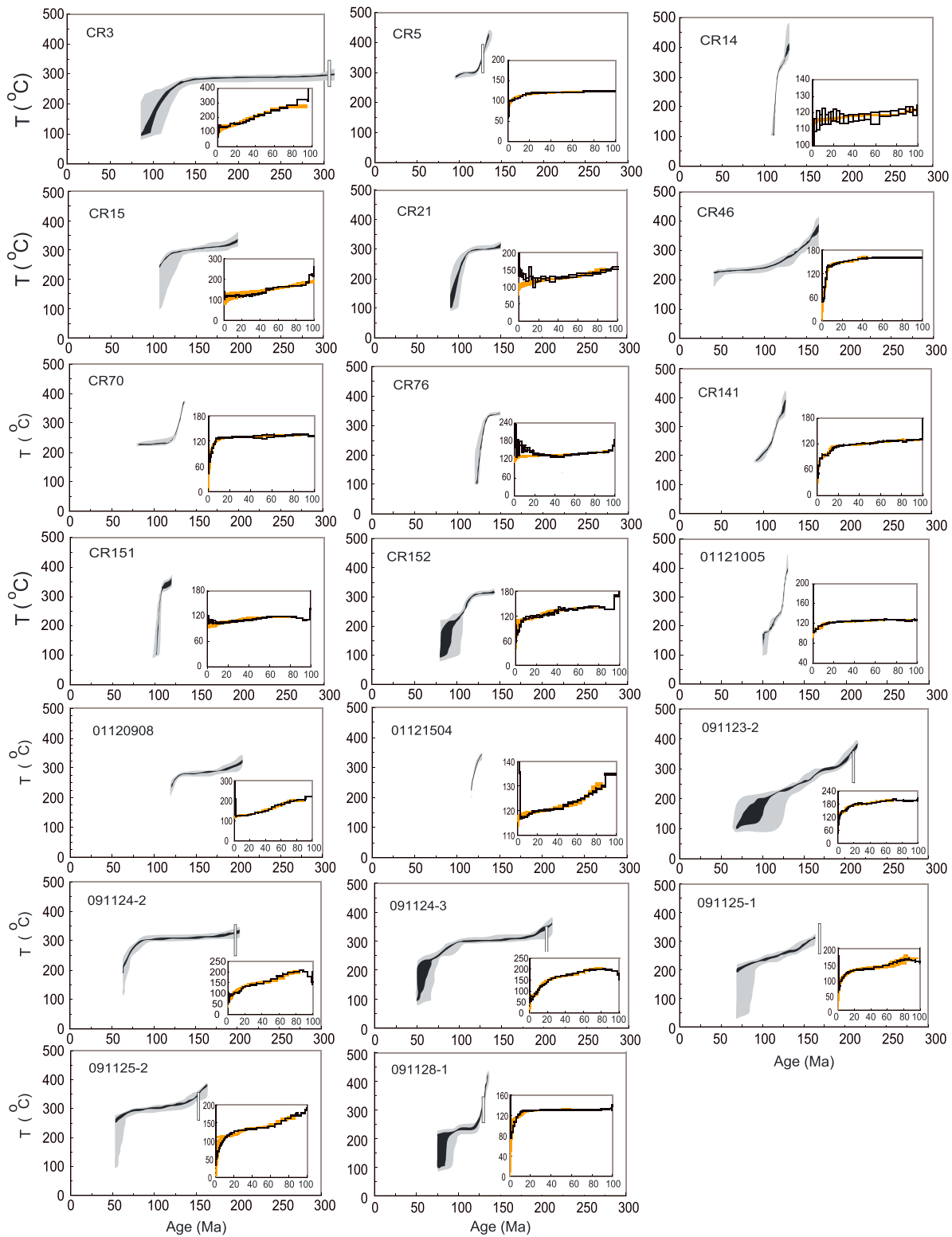


Figure 8. Modeled cooling histories for all the K-feldspars. The light shadow covers a 90% confident interval of the distribution of the 50 calculated cooling histories and its 90% confident interval median are observed (dark shadow). The inset shows the fit of the 50 modeled age spectra (orange red lines) with the experimental age spectrum (black line). The x axis of the inset is the cumulative ^{39}Ar in percent (%), and the y axis is age in Ma.

Table 2. The Activation Energies and Frequency Factors ($\log(D_0/r_0^2)$) Used for MDD Modeling

Sample	E (kJ/mol)	$\log(D_0/r_0^2)$ (s^{-1})
CR3	159.5 ± 11.1	4.6 ± 0.8
CR5	192.2 ± 14.8	4.1 ± 1.0
CR14	248.7 ± 15.6	9.0 ± 1.0
CR15	260.0 ± 1.4	9.8 ± 1.5
CR21	263.3 ± 19.3	9.6 ± 1.3
CR46	249.1 ± 13.1	9.0 ± 0.9
CR70	232.4 ± 12.3	8.0 ± 0.8
CR76	176.3 ± 4.9	4.4 ± 0.3
CR141	243.3 ± 15.2	9.6 ± 1.0
CR151	259.6 ± 10.3	8.7 ± 0.7
CR152	164.5 ± 7.0	4.5 ± 0.5
01121005	319.5 ± 20.5	11.8 ± 1.3
01120908	244.1 ± 9.0	8.9 ± 0.6
01121504	189.7 ± 8.6	5.7 ± 0.6
091123-2	177.1 ± 10.3	4.9 ± 0.7
091124-2	194.7 ± 13.1	5.8 ± 0.9
091124-3	201.8 ± 13.5	6.8 ± 0.9
091125-1	269.6 ± 14.4	10.4 ± 1.0
091125-2	278.0 ± 15.6	10.8 ± 1.0
091128-1	275.1 ± 20.5	10.1 ± 1.4

Outputs from the automated MDD modeling routines fit well the experimental results of Arrhenius data (Figures 7A–7H, red square and black solid diamond) and $\log(r/r_0)$ plots (Figures 7a–7h), suggesting that the assumed parameters can faithfully reflect the “true” situation of the diffusion kinetics [e.g., *Lovera et al.*, 1989, 1991; *Cassata and Renne*, 2013].

Experimental age spectra also fit well (insets in Figure 8) vis-à-vis the modeled ones after appropriate adjustment of the various model parameters. Except 01121005, the activation energies (E) and frequency factors ($\log(r/r_0)$) are in ranges of 278.0–159.5 kJ and 4.1–10.8 s^{-1} , respectively (Table 2); both are in the normal ranges [*McDougall and Harrison*, 1999]. It seems that the samples having locality affiliation hold similar factors (Tables 1 and 2). The abnormal high E (319.5 ± 20.5 kJ) and $\log(r/r_0)$ (11.8 ± 1.3 s^{-1}) (Table 2) of 01121005 suggest a small degas at the low-temperature portion of the step heating, for which the reason is unclear.

Cooling histories then can be obtained from the modeling for the samples from the NCC and YTC. The details are described in Appendix S3. The cooling histories of the 20 K-feldspars are shown graphically in Figure 8. They appear to be consistent with the biotite $^{40}Ar/^{39}Ar$ data (closure temperature 280–380°C) [*Harrison et al.*, 1985; *Grove and Harrison*, 1996]. The cooling histories for all the samples are collectively shown in Figures 9a and 9b for the NCC and YTC, respectively. Also shown are the apatite fission track ages from literatures [*Hu et al.*, 2006; *Zhang et al.*, 2002; *Qing et al.*, 2008; *Ding et al.*, 2011; *Shen et al.*, 2012].

At one glance at Figure 9, there is a strong contrast in cooling patterns between the NCC and YTC, and both are similar to their average cooling patterns (Figure 5). Except CR46 (blue line in Figure 9), cooling histories of samples from NCC show two types of cooling patterns: (1) cooling rapidly from ~400 to ~150°C from ~125 to ~100 Ma (Figure 9a), such as for CR151, CR14, and 01121005 (Figures 8 and 9a); (2) two-stage cooling patterns characterized by a first rather slow cooling period (~0.4°C/Ma)

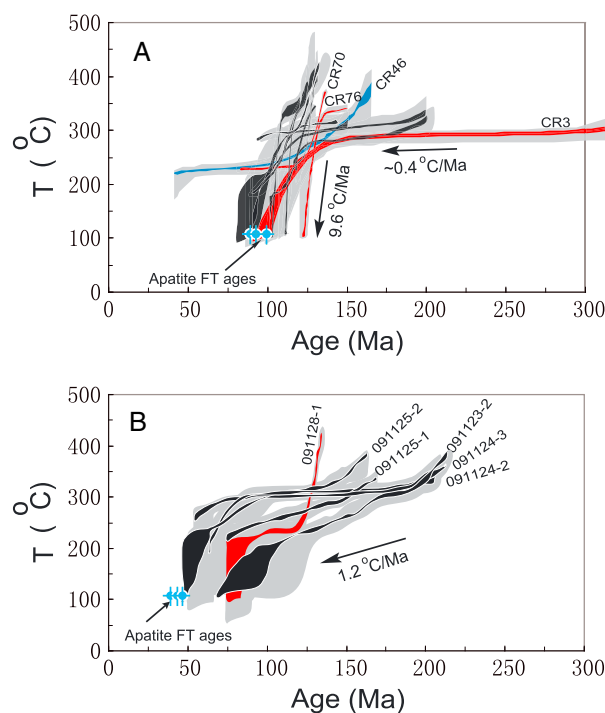


Figure 9. Compiled cooling histories for the upper crusts of the (a) NCC and (b) YTC, respectively. A strong contrast between the NCC and YTC is identified. A rapid cooling event can be defined during 125–100 Ma from ~400 to ~150°C yielding an average cooling rate of ~9.6°C/Ma for the NCC. The fission track data collected from the corresponding localities are also shown [*Hu et al.*, 2006; *Zhang et al.*, 2002; *Qing et al.*, 2008; *Ding et al.*, 2011; *Shen et al.*, 2012], which are quite consistent with the cooling paths. In contrast, over a long period from ~200 to ~70 Ma, cooling histories of samples from the YTC, except 091128-1 (red line in Figure 9b), are mostly characterized by a gentle and slow cooling feature with an average rate of ~1.2°C/Ma. The fission track data collected from the corresponding localities are consistent with the cooling trend. See text for details.

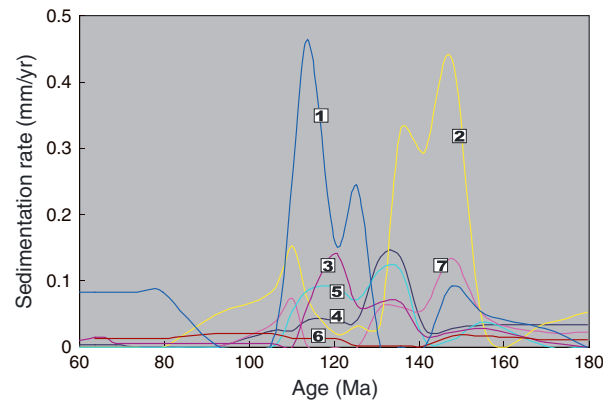


Figure 10. Sedimentation rates of different locations on the NCC that were calculated from the original data by Wang and Chen, 2005. The numbers are similar to those in Figure 2. Overall, the rates were stable before 155 Ma and increased apparently during ~150–105 Ma. Shandong (eastern NCC) exhibits an abnormally high sedimentation rate of ~130 Ma and peaked at 115 Ma. West Beijing displayed an abruptly increased sedimentation rate during 150–130 Ma and peaked at ~145 Ma. The sedimentation rate on the west NCC stayed low during the entire Late Mesozoic.

followed by a sudden increased cooling event, such as for CR3, CR152, and CR21 (Figures 8 and 9a). The shifts from slow to rapid cooling events of CR152 and CR21 roughly began at ~125 Ma (Figures 9 and 10a). Therefore, a rapid cooling event can be identified during 125–100 Ma from ~400 to ~150°C yielding an average cooling rate of ~9.6°C/Ma. The cooling trend is substantiated by the fission track data (closure temperature 110°C) collected from the central and eastern NCC, of which the earliest ages concentrate in a range of ~95–102 Ma [Hu *et al.*, 2006; Zhang *et al.*, 2002; Qing *et al.*, 2008; Ding *et al.*, 2011] that are quite consistent with the cooling paths (Figure 9a). It seems that CR70 and CR76 (red line in Figure 9) cooled earlier than others starting at ~135 Ma (Figure 9a). Although at a low resolution, CR3 (red line) shifted from a long slow cooling period (~0.4°C/Ma) to a rapid cooling event at ~135 Ma (Figure 9a), suggesting it remained stable for a long time

before the rapid unroofing event began at 135 Ma. Considering that CR70, CR76, and CR3 are all from the northern portion of NCC, this implies that the northern parts of the NCC cooled earlier than the central and eastern part of the NCC. This feature is reflected by the sedimentation rates on NCC (see discussion later). CR46, collected from the western part of NCC, shows a different cooling history (blue line in Figure 9a) from those of either the north or east of NCC. It cooled from 160 Ma down to ~50 Ma at a gentle slope and shows no distinct inflection.

In contrast, over a long period from ~200 to ~70 Ma, cooling histories of samples from the YTC, except 091128–1 (red line in Figure 9b), are mostly characterized by a gentle and slow cooling feature with an average cooling rate of ~1.2°C/Ma (Figure 9b). The cooling trend is also substantiated by the fission track data collected from the same plutons [Shen *et al.*, 2012], suggesting that the cooling paths are reasonable (Figure 9b). Sample 091128–1 provides a distinct cooling history from the rest of the samples from YTC (red line in Figure 9b). It is characterized by a rapid cooling period between 130 Ma and 120 Ma followed by a slow cooling period and then a rapid cooling period. This cooling pattern is rather similar to those from the Dabie plutons, implying that the sample was affected by the Dabie orogeny because of the proximity of locality.

Structural or thermal expansion regime changes may occur in K-feldspar crystals during step-heating experiment [Cassata and Renne, 2013]. These changes cause inaccuracy in thermal history of MDD model. The calculation illustrates that at a given time, the predicted temperature using MDD model could exceed the true temperature up to 40°C [Cassata and Renne, 2013]. However, this is not important in this study, because our concern is the contrast in cooling patterns between the upper crusts of the NCC and YTC, and the accurate cooling rates is less important.

6. Contrast Unroofing Patterns Between the NCC and YTC

The cooling histories obtained may be the result from either unroofing or argon loss by later reheating. It is difficult to imagine that an area as enormous as the NCC or YTC was reheated to 150–450°C so that the K-feldspar was impressed. This is because, first, there is a lack of widespread magmatism or volcanism after the Late Mesozoic, and second, the undeformed feature of the granitoids (granites, adamellites, syenites, and diorites) implies that they were not impacted by the later metamorphic activity (thermal event). Therefore, we prefer to state that the cooling histories observed above reflect the unroofing process rather than later reheating. Therefore, we conclude that the upper crusts of the NCC and YTC had experienced completely different unroofing processes during the Late Mesozoic.

7. Implications for the Geodynamic Setting of Eastern Asian Continent

The discussion above indicates that the crust was thinner in the Cretaceous than in the Jurassic, and a relatively rapid unroofing event occurred on the NCC contrasting clearly with the YTC. So, what is the mechanism behind these phenomena?

Several hypotheses have been proposed to explain the lithospheric destruction of the NCC and YTC, such as delamination [Deng *et al.*, 1994; Gao *et al.*, 2002; Wu *et al.*, 2005], thermal erosion [Griffin *et al.*, 1998; Xu *et al.*, 2004, 2009, 2007; Xu, 2007; Zhang *et al.*, 2003; Zheng *et al.*, 2001, 2007; Menzies *et al.*, 2007], and melt-peridotite interaction [Zhang *et al.*, 2003; Tang *et al.*, 2008].

Thermal erosion mechanism was inspired from a seismic image of the “mushroom cloud” beneath the North China craton [Griffin *et al.*, 1998; Menzies *et al.*, 2007]. It states that the lower lithosphere was baked and softened by the hot upwelling asthenosphere, and finally, it turned into a part of the asthenosphere mechanically, thereby causing the gradual thinning of the lithosphere [Xu, 2007]. Melt-peridotite interaction hypothesis argues that the chemical reaction between the peridotite and melt might be the mechanism of the lithospheric destruction below the NCC [Zhang *et al.*, 2003; Tang *et al.*, 2008]. Geochemically, the lithosphere of the NCC varied during the Paleozoic, Mesozoic, and Cenozoic, which could be a result of the chemical reaction [Zhang *et al.*, 2003].

Delamination of the lithospheric mantle allows losing the root of the lithosphere and bringing the hot asthenosphere in contact with the Moho [Bird, 1979]. This predicts massive magmatism and uplift of the crust resulting in an extensional response in the shallow crust. Especially, the thinned crust of the NCC can be explained by the delamination together with the lithosphere [Wu *et al.*, 2005]. One of the direct evidences suggests that the old lithosphere was replaced by a newer one completely sometime before the Cenozoic [Gao *et al.*, 2002]. It is a prevailing view that the paleo-Pacific plate subducted northwestward beneath the Asian continent during the Mesozoic [Griffin *et al.*, 1998; Davis *et al.*, 2001; Wu *et al.*, 2005], which resulted in lithospheric thickening and subsequently, lithospheric removal in the eastern NCC [Griffin *et al.*, 1998; Wu *et al.*, 2005]. The question is, did the NCC delaminate together with the YTC?

It has been recognized that the NCC was characterized by lithospheric thinning during the Late Mesozoic, which may have resulted from the northwestward subduction of the paleo-Pacific plate [e.g., Fan and Menzies, 1992; Griffin *et al.*, 1992, 1998; Gao *et al.*, 2002; Wu *et al.*, 2005; Menzies *et al.*, 2007; Zheng *et al.*, 2007; Zhu *et al.*, 2012b] although its mechanism and process are still controversial [e.g., Gao *et al.*, 2002; Zhang *et al.*, 2003; Wu *et al.*, 2005; Zheng *et al.*, 2007]. Several lines of evidences show that the reactivation of the NCC occurred at the northern margin as early as the Late Paleozoic but peaked during the Early Jurassic, which involved extensive magmatism, deformation, and exhumation of the cratonic basement [Wang *et al.*, 2013b]. A super mantle plume around ~125 Ma [Larson, 1991] might be the cause of intensified delamination of the NCC at that time. It has been proposed that the mid-Cretaceous mid-Pacific super-plume increased subduction rates at its outer margins, which may have assisted the lithospheric delamination in eastern China [Wu *et al.*, 2005]. Although the Cretaceous magmatism was widespread in the northern and eastern NCC, the Jurassic magmatism was confined along the northern margin of the NCC [Wu *et al.*, 2005].

Continental facies dominate the sedimentation on the NCC during the Jurassic and Cretaceous [Wang and Chen, 2005]. Unroofing could be mirrored by continental sedimentation. Figure 10 shows sedimentation rates from a number of localities on the NCC. Overall, sedimentation rates maintained a low and stable value before 155 Ma and increased apparently during ~150–105 Ma implying increased unroofing. Shandong (the eastern NCC) exhibits abnormally high sedimentation rate from ~130 Ma that peaked at 115 Ma (Line 1 in Figures 10 and 2), reflecting intensified unroofing at that time. The location west of Beijing in the northwest of the NCC displayed an abrupt increase in sedimentation rate during 150–130 Ma that peaked at ~145 Ma (Line 2 in Figures 10 and 2) suggesting that the unroofing occurred ~15 Myr earlier than in the eastern NCC. This observation is quite consistent with the earlier cooling in the northern part of the NCC indicated by CR3, CR70, and CR76 (Figure 9a) (see discussion above), suggesting that the northern part of the NCC was delaminated earlier than the eastern NCC. Relatively, the sedimentation on the west NCC had a low profile implying that the unroofing was not as strong as that on the eastern NCC during the Late Mesozoic.

Detailed geochemical and geophysical studies have indicated that intensive structural deformation and low seismic wave velocities in the upper mantle currently characterize the eastern NCC [Griffin *et al.*, 1998;

Wu *et al.*, 2005; Xu, 2007; Zheng *et al.*, 2007; Chen *et al.*, 2008a, 2008b; Yang *et al.*, 2008; Chen, 2010; Zhu *et al.*, 2012b]. Moreover, studies on mantle xenoliths in the Tertiary alkali basalts indicate that the lithospheric mantle beneath the eastern NCC is thin, fertile, hot, and of high density in contrast with the cratonic lithospheric mantle recorded by the mantle xenoliths in the mid-Ordovician (ca. 480 Ma) [Li *et al.*, 2011] kimberlites [Griffin *et al.*, 1998; Gao *et al.*, 2002; Xu, 2007]. These observations suggest that the eastern NCC was destroyed sometime between the mid-Ordovician and Tertiary.

The Late Mesozoic magmatism is prominent (Figure 5) in the NCC. This widespread magmatism (135–110 Ma) [Wu *et al.*, 2005, and references therein] was taken as a sign of lithospheric destruction [Wu *et al.*, 2005]. Detailed geochemical and isotopic researches, especially in situ zircon Hf isotope data illustrate that these magmas were derived from various sources including depleted mantle, enriched lithospheric mantle, ancient lower crust, and juvenile crust suggesting intensive mantle-crust interaction during their formation [Chen *et al.*, 2008a, 2008b; Yang *et al.*, 2008; Chen, 2010]. The transition from enriched to depleted mantle sources for the mafic magmas indicates that the thick cratonic lithospheric mantle beneath the eastern NCC was significantly removed or replaced by a juvenile lithospheric mantle [Gao *et al.*, 2002]. This is also supported by studies on mantle xenoliths in the Meso-Cenozoic alkali basalts [Zheng *et al.*, 2007, and references therein].

Extensional structures are popular throughout the NCC, including detachment faults, metamorphic core complexes, fault bounded basins, and dyke swarms as a major response to lithospheric thinning in the shallow crust [Meng, 2003; Liu *et al.*, 2008, 2013; Lin and Wang, 2006; Yang *et al.*, 2008; Li *et al.*, 2012]. The transition of the tectonic regime from contraction to extension occurred at the beginning of the Cretaceous [Davis *et al.*, 2001; Lin *et al.*, 2013]. Early Cretaceous metamorphic core complexes were reported in Liaonan, Yiwulvshan, Yunmengshan, Miyun, Chengde, Hohhot, and Sulu [Davis *et al.*, 2001; Meng, 2003; Liu *et al.*, 2006; Lin and Wang, 2006; Lin *et al.*, 2013; Yang *et al.*, 2008]. These metamorphic core complexes are characterized by synchronous denudation (135–115 Ma) and have a uniform movement direction (NWW-SEE). The age of detachment faults that controlled the Yiwulvshan and Louzidian-Dachengzi metamorphic complexes in Liaoxi is 127–116 Ma and 133–118 Ma, respectively [Rutshstein, 1992; Zhang *et al.*, 2002]. Early Cretaceous fault basins (pull-apart basins) including Chengde, Fuxin, Jiaolai, and Hefei basins are also widely developed in the eastern NCC [Zhu *et al.*, 2012a, 2012b]. A common feature shared by these basins is that they are controlled by extensional normal or detachment faults [Meng, 2003; Li *et al.*, 2012; Liu *et al.*, 2013]. Although these faults have different trends, their hanging walls exhibit consistent directions of movement implying that they formed in a uniform tectonic regime. Dyke swarms are products of typhonic magmatism that might provide important information of the deep. Several dyke swarms have been reported including Gufeng lamprophyre dykes (146.6 ± 2.9 Ma, K-Ar age on biotite) [Ying *et al.*, 2004], Linxi diabasic dykes (100.6 ± 2.7 Ma, K-Ar age on biotite) [Shao *et al.*, 1998], Sulu mafic dykes (from 120.3 ± 2.1 to 126.9 ± 1.9 Ma) [Liu *et al.*, 2008], and north Beijing bimodal dykes (114–124 Ma, K-Ar age on biotite) [Shao *et al.*, 1998].

The rapid unroofing event on the NCC observed in this study can be explained by lithospheric mantle delamination. Delamination usually results in a sudden uplift of the crust [Bird, 1979] and unroofing ensues. The sedimentation rates and cooling histories show that the unroofing process at northern portion of the NCC started earlier than the central and eastern portion, and the western NCC probably did not suffer the same process. These observations imply that the thinning or destruction in the NCC lithosphere may have initiated in the northern part (~140–135 Ma) and intensified subsequently and spread throughout the whole of eastern NCC (~125 Ma).

As a contrast to the NCC, the cooling history of the upper crust of the YTC shows a gentle and relatively constant cooling rate (~1.2°C/Ma, Figure 9b) suggesting that there was no rapid unroofing event during 200–75 Ma. This is consistent with the observation from the YTC in terms of deformation and magmatism during the Mesozoic. Although metamorphism is poorly observed for the Mesozoic rock package, it could be commonly identified and generally shows a low metamorphic grade in the central YTC [Wang *et al.*, 2013c, and references therein]. Late Mesozoic magmatism is not developed in the central and eastern YTC [Chu *et al.*, 2012a, 2012b; Wang *et al.*, 2013c] but occurred locally north of it, which might be a result of the Dabie orogeny. Recent studies suggest that the Xuefengshan range, in eastern YTC, is a Triassic intracontinental orogen, which was relatively quiet during the Late Mesozoic [Faure *et al.*, 2009; Charvet *et al.*, 2010; Li *et al.*, 2010; Chu *et al.*, 2012a, 2012b; Wang *et al.*, 2013c]. Therefore, although a thin crust is also identified for the YTC at present by geophysical data suggesting it was also thinned at some time, it is unlikely to have happened during 200–75 Ma. The above

geochronological data show that the crust was still thick by the Late Jurassic. Therefore, we prefer to state that the lithospheric thinning of the YTC might have happened after 75 Ma. This is consistent with the observations of the recent thermochronological studies [Li and Shan, 2011; Shen et al., 2012], which have indicated that the rapid cooling and exhumation events occurred throughout the YTC after ~96 Ma.

8. Conclusions

High-resolution $^{40}\text{Ar}/^{39}\text{Ar}$ analyses were conducted on K-feldspars and biotites from the plutonic and metamorphic rocks of Mesozoic age or older from the NCC and YTC. Contrast cooling patterns between the upper crusts of the NCC and YTC were identified. On the NCC, cooling is more rapid than on the YTC. After checking a number of mechanisms, our observations can be explained by the lithospheric delamination model. Together with the sedimentation rates over the NCC, we argue that the lithospheric thinning initiated from the northern portion around 140–135 Ma and spread to the central and eastern portions gradually during 125–100 Ma.

In contrast, a slower cooling period was observed during 200–75 Ma on the YTC, which is consistent with observations of weak magmatism and relatively quiet tectonic activity during the Cretaceous. Nevertheless, the thinned modern lithosphere implies that it was also destructed at some time. The crust of the YTC in the Late Triassic was thicker than that of the NCC in the Cretaceous, which implied by the pure conductive cooling. Therefore, we conclude that the lithospheric thinning of the YTC perhaps happened after ~75 Ma.

Acknowledgments

We would like to thank Sunlin Chung and Oscar M. Lovera for their reviews and constructive suggestions. Editorial comments by Tom Parsons and the Associate Editor are very gratefully acknowledged. This study is jointly funded by the China Natural Science Foundation (90714007, 41025010, and 41221002) and the “Strategic Priority Research Program” of the Chinese Academy of Sciences (XDB03020203 and KZCX2-YW-Q08-3).

References

- Ai, Y., and T. Y. Zheng (2003), The upper mantle discontinuity structure beneath eastern China, *Geophys. Res. Lett.*, *30*(B11), 2089, doi:10.1029/2003GL017678.
- Arnaud, N. O., and S. P. Kelley (1997), Argon behaviour in gem-quality orthoclase from Madagascar: Experiments and some consequences for $^{40}\text{Ar}/^{39}\text{Ar}$ geochronology, *Geochim. Cosmochim. Acta*, *61*, 3227–3255, doi:10.1016/S0016-7037(97)00152-X.
- Bureau of Geology and Mineral Resources of Nei Mongolia Autonomous Region (BGMRNM) (1991), *Regional Geology of Nei Mongolia Autonomous Region* [in Chinese], 725 pp., Geological Publishing House, Beijing.
- Bird, P. (1979), Continental delamination and the Colorado Plateau, *J. Geophys. Res.*, *84*, 7561–7571, doi:10.1029/JB084iB13p07561.
- Cassata, W. S., and P. R. Renne (2013), Systematic variations of argon diffusion in feldspars and implications for thermochronometry, *Geochim. Cosmochim. Acta*, *112*, 251–287, doi:10.1016/j.gca.2013.02.030.
- Charvet, J., L. S. Shu, M. Faure, F. Choulet, B. Wang, H. F. Lu, and N. Le Breton (2010), Structural development of the Lower Paleozoic belt of South China: Genesis of an intracontinental orogen, *J. Asian Earth Sci.*, *39*, 309–330, doi:10.1016/j.jseas.2010.03.006.
- Chen, L. (2010), Concordant structural variations from the surface to the base of the upper mantle in the North China Craton and its tectonic implications, *Lithos*, *120*, 96–115, doi:10.1016/j.lithos.2009.12.007.
- Chen, B., W. Tian, B. M. Jahn, and Z. C. Chen (2008a), Zircon SHRIMP U–Pb ages and in-situ Hf isotopic analysis for the Mesozoic intrusions in South Taihang, North China craton: Evidence for hybridization between mantle-derived magmas and crustal components, *Lithos*, *102*, 118–137, doi:10.1016/j.lithos.2007.06.012.
- Chen, L., T. Wang, L. Zhao, and T. Y. Zheng (2008b), Distinct lateral variation of lithospheric thickness in the northeastern North China Craton, *Earth Planet. Sci. Lett.*, *267*, 56–68, doi:10.1016/j.epsl.2007.11.024.
- Cherniak, D. J., and E. B. Watson (2000), Pb diffusion in zircon, *Chem. Geol.*, *172*, 5–24, doi:10.1016/S0009-2541(00)00233-3.
- Chi, J., and F. X. Lu (1992), *Cenozoic Basalts and Upper Mantle in Eastern China*, 57 pp., China Geosciences Univ. Press, Wuhan, China.
- Chu, Y., W. Lin, M. Faure, C. Q. Wang, and W. B. Ji (2012a), Phanerozoic tectonothermal events of the Xuefengshan Belt, central South China: Implications from U–Pb age and Lu–Hf determinations of granites, *Lithos*, *150*, 243–255, doi:10.1016/j.lithos.2012.04.005.
- Chu, Y., M. Faure, Q. C. Wang, and W. B. Ji (2012b), Tectonics of the Middle Triassic intracontinental Xuefengshan Belt, South China: New insights from structural and chronological constraints on the basal décollement zone, *Int. J. Earth Sci.*, *101*, 2125–2150, doi:10.1007/s00531-012-0780-5.
- Davis, G. A., Y. Zheng, C. Wang, B. J. Darby, C. Zhang, and G. Gehrels (2001), Mesozoic tectonic evolution of the Yanshan fold and thrust belt, with emphasis on Hebei and Liaoning provinces, Northern China, in *Paleozoic and Mesozoic Tectonic Evolution of Central Asia: From Continental Assembly to Intracontinental Deformation*, vol. 194, edited by M. S. Hendrix and G. A. Davis, pp. 171–198, Geological Society of America Memoir, Boulder, Colo., doi:10.1130/0-8137-1194-0.171.
- Deng, J. F., X. X. Mo, H. L. Zhao, Z. H. Luo, and Y. S. Du (1994), Lithosphere root/de-rooting and reactivation of the eastern China continent [in Chinese with English abstract], *Geoscience*, *8*, 349–356.
- Ding, C., G. Chen, Z. Li, X. Mao, and F. Yang (2011), Apatite fission track analysis of tectono-thermal history in the northeast of Ordos Basin [in Chinese with English abstract], *Geosciences*, *25*, 581–588, doi:10.3969/j.issn.1000-8527.2011.03.021.
- Dodson, M. H. (1973), Closure temperature in cooling geochronological and petrological systems, *Contrib. Mineral. Petrol.*, *40*, 259–274.
- Fan, Q. C., and P. R. Hooper (1989), The mineral chemistry of ultramafic xenoliths of eastern China: Implications for upper mantle composition and the paleogeotherms, *J. Petrol.*, *30*, 1117–1158, doi:10.1093/petrology/30.5.1117.
- Fan, W. M., and M. A. Menzies (1992), Destruction of aged lower lithosphere and accretion of asthenosphere mantle beneath eastern China, *Geotectonic Metallogeny*, *16*, 171–180.
- Faure, M., L. S. Shu, B. Wang, J. Charvet, F. Choulet, and P. Monie (2009), Intracontinental subduction: A possible mechanism for the Early Palaeozoic Orogen of SE China, *Terra Nova*, *21*, 360–368, doi:10.1111/j.1365-3121.2009.00888.x.
- Gao, S., R. L. Rudnick, R. W. Carlson, W. F. McDonough, and Y. S. Liu (2002), Re–Os evidence for replacement of ancient mantle lithosphere beneath the North China Craton, *Earth Planet. Sci. Lett.*, *198*, 307–322, doi:10.1016/S0012-821X(02)00489-2.

- Gao, S., R. L. Rudnick, H. L. Yuan, X. M. Liu, Y. S. Liu, W. L. Xu, W. L. Ling, J. Ayers, X. C. Wang, and Q. H. Wang (2004), Recycling lower continental crust in the North China Craton, *Nature*, *432*, 892–897, doi:10.1038/nature03162.
- Griffin, W. L., S. Y. O'Reilly, and C. G. Ryan (1992), Composition and thermal structure of the lithosphere beneath South Africa, Siberia and China: Proton microprobe studies, Abstract of the International Symposium on Cenozoic Volcanic Rocks and Deep-seated Xenoliths of China and its Environs, Beijing, 65–66.
- Griffin, W. L., A. Zhang, S. Y. O'Reilly, and C. G. Ryan (1998), Phanerozoic evolution of the lithosphere beneath the Sino-Korean Craton, in *Mantle Dynamics and Plate Interaction in East Asia, Geodynamics Series*, vol. 27, edited by M. F. J. Flower et al., pp. 107–126, AGU, Washington, D. C., doi:10.1029/GD027p0107.
- Grove, M., and T. M. Harrison (1996), $^{40}\text{Ar}^*$ diffusion in Fe-rich biotite, *Am. Mineral.*, *81*, 940–951.
- Hall, C. M., R. C. Walter, J. A. Westgate, and D. York (1984), Geochronology, stratigraphy and geochemistry of Cindery Tuff in Pliocene hominid-bearing sediments of the Middle Awash, Ethiopia, *Nature*, *308*, 26–31, doi:10.1038/308026a0.
- Han, B. F., H. Kagami, and H. M. Li (2004), Age and Nd-Sr isotopic geochemistry of the Guangtoushan alkaline granite, Hebei Province, China: Implications for early Mesozoic crust-mantle interaction in North China Block [in Chinese with English abstract], *Acta Petrologica Sinica*, *20*, 1375–1388.
- Harrison, T. M., I. Duncan, and I. McDougall (1985), Diffusion of ^{40}Ar in biotite: Temperature, pressure and compositional effects, *Geochim. Cosmochim. Acta*, *49*, 2461–2468, doi:10.1016/0016-7037(85)90246-7.
- Hu, S., A. Raza, K. Min, B. Kohn, P. W. Reiners, R. A. Ketchum, J. Y. Wang, and A. J. W. Gleadow (2006), Late Mesozoic and Cenozoic tectonic evolution along a transect from the north China craton through the Qinling Orogen into the Yangtze craton, *Tectonics*, *25*, TC6009, doi:10.1029/2006TC001985.
- Larson, R. L. (1991), Latest pulse of Earth: Evidence for a mid-Cretaceous superplume, *Geology*, *19*, 547–550, doi:10.1130/0091-7613(1991)019.
- Lee, J. K. W. (1995), Multipath diffusion in geochronology, *Contrib. Mineral. Petrol.*, *120*, 60–82, doi:10.1007/BF00311008.
- Li, X. M., and Y. H. Shan (2011), Diverse exhumation of the Mesozoic tectonic belt within the Yangtze Plate China, determined by apatite fission-track thermochronology, *Geosci. J.*, *15*, 349–357, doi:10.1007/s12303-011-0037-5.
- Li, Z. X., X. H. Li, J. A. Wartho, C. Clark, W.-X. Li, C. L. Zhang, and C. Bao (2010), Magmatic and metamorphic events during the early Paleozoic Wuyi–Yunkai orogeny, southeastern South China: New age constraints and pressure–temperature conditions, *Geol. Soc. Am. Bull.*, *122*, 772–793, doi:10.1130/B30021.1.
- Li, Q. L., F. Y. Wu, X. H. Li, Z. L. Qiu, Y. Liu, Y. H. Yang, and G. Q. Tang (2011), Precisely dating Paleozoic kimberlites in the North China Craton and Hf isotopic constraints on the evolution of the subcontinental lithospheric mantle, *Lithos*, *126*, 127–134, doi:10.1016/j.lithos.2011.07.001.
- Li, S. Z., G. C. Zhao, L. M. Dai, X. Liu, L. H. Zhou, M. Santosh, and Y. H. Suo (2012), Mesozoic basins in eastern China and their bearing on the deconstruction of the North China Craton, *J. Asian Earth Sci.*, *47*, 64–79, doi:10.1016/j.jseas.2011.06.008.
- Lin, W., and Q. C. Wang (2006), Late Mesozoic extensional tectonics in the North China block: A crustal response to subcontinental mantle removal?, *Bull. Soc. Geol. France*, *177*, 287–297, doi:10.2113/gssgfbull.177.6.287.
- Lin, W., Y. Faure, Y. Chen, W. Ji, F. Wang, L. Wu, N. Charles, J. Wang, and Q. Wang (2013), Late Mesozoic compressional to extensional tectonics in the Yiwulvshan massif, NE China and its bearing on the evolution of the Yinshan-Yanshan orogenic belt: Part I: Structure analyses and geochronological constraints, *Gondwana Res.*, *23*, 54–77, doi:10.1016/j.jgr.2012.02.013.
- Liu, J. L., H. M. Guan, and L. Hu (2006), Late Mesozoic metamorphic core complexes: New constraints on lithosphere thinning in North China, *Prog. Nat. Sci.*, *16*, 633–638.
- Liu, S., R. Z. Hu, S. Gao, C. X. Feng, Y. Q. Qi, T. Wang, G. Y. Feng, and I. M. Coulson (2008), U–Pb zircon age, geochemical and Sr–Nd–Pb–Hf isotopic constraints on age and origin of alkaline intrusions and associated mafic dikes from Sulu orogenic belt Eastern China, *Lithos*, *106*, 356–379, doi:10.1016/j.lithos.2008.09.004.
- Liu, S. F., S. Su, and G. W. Zhang (2013), Early Mesozoic basin development in North China: Indications of cratonic deformation, *J. Asian Earth Sci.*, *62*, 221–236, doi:10.1016/j.jseas.2012.09.011.
- Lovera, O. M., F. M. Richter, and T. M. Harrison (1989), The $^{40}\text{Ar}/^{39}\text{Ar}$ thermochronology for slowly cooled samples having a distribution of diffusion domain sizes, *J. Geophys. Res.*, *94*, 17,917–17,935, doi:10.1029/JB094iB12p17917.
- Lovera, O. M., F. M. Richter, and T. M. Harrison (1991), Diffusion domains determined by ^{39}Ar released during step heating, *J. Geophys. Res.*, *96*, 2057–2069, doi:10.1029/90JB02217.
- Lovera, O. M., M. Grove, T. M. Harrison, and K. I. Mahon (1997), Systematic analysis of K-feldspar $^{40}\text{Ar}/^{39}\text{Ar}$ step heating results I: Significance of activation energy determinations, *Geochim. Cosmochim. Acta*, *61*, 3171–3192, doi:10.1016/S0016-7037(97)00147-6.
- Lovera, O. M., M. Grove, and T. M. Harrison (2002), Systematic analysis of K-feldspar $^{40}\text{Ar}/^{39}\text{Ar}$ step heating results II: Relevance of laboratory argon diffusion properties to nature, *Geochim. Cosmochim. Acta*, *66*, 237–1255, doi:10.1016/S0016-7037(01)00846-8.
- Ma, L. F. (2002), *Geological Map of China* [in Chinese], Geological Press, Beijing.
- McDougall, I., and T. M. Harrison (1999), *Geochronology and Thermochronology by the $^{40}\text{Ar}/^{39}\text{Ar}$ Method*, Oxford Univ. Press, Oxford, New York.
- McLaren, S., and S. M. Reddy (2008), Automated mapping of K-feldspar by electron backscatter diffraction and application to $^{40}\text{Ar}/^{39}\text{Ar}$ dating, *J. Struct. Geol.*, *30*, 1229–1241, doi:10.1016/j.jsg.2008.05.008.
- Meng, Q. (2003), What drove Late Mesozoic extension of the northern China–Mongolia tract?, *Tectonophysics*, *369*, 155–174, doi:10.1016/S0040-1951(03)00195-1.
- Menzies, M., Y. G. Xu, H. F. Zhang, and W. M. Fan (2007), Integration of geology, geophysics, and geochemistry: A key to understanding the North China Craton, *Lithos*, *96*, 1–21, doi:10.1016/j.lithos.2006.09.008.
- Mock, C., N. O. Arnaud, J. M. Cantagrel, and G. Yirgu (1999), $^{40}\text{Ar}/^{39}\text{Ar}$ thermochronology of the Ethiopian and Yemeni basements: Reheating related to the Afar plume?, *Tectonophysics*, *314*, 351–372, doi:10.1016/S0040-1951(99)00224-3.
- Parsons, I., K. A. Waldron, F. D. L. Walker, R. Burgess, and S. P. Kelley (1991), Microstructural controls of ^{40}Ar loss and ^{18}O exchange in alkali feldspars, *EOS Trans. AGU*, *72*, 290.
- Parsons, I., W. L. Brown, and J. V. Smith (1999), $^{40}\text{Ar}/^{39}\text{Ar}$ thermochronology using alkali feldspar: Real thermal history or mathematical mirage of microtexture?, *Contrib. Mineral. Petrol.*, *136*, 92–110, doi:10.1007/s004100050526.
- Parsons, I., J. D. F. Gerald, M. T. Heizler, L. L. Heizler, T. Ivanic, and M. R. Lee (2013), Eight-phase alkali feldspars: Low-temperature cryptoperthite, peristerite and multiple replacement reactions in the Klokken intrusion, *Contrib. Mineral. Petrol.*, *165*, 931–960, doi:10.1007/s00410-012-0842-5.
- Qing, J. C., J. Ji, J. D. Wang, Q. L. Peng, X. L. Niu, and Z. H. Ge (2008), Apatite fission track study of Cenozoic uplifting and exhumation of Wutai Mountain, China., *Chin. J. Geophys.*, *51*, 384–392, doi:10.1002/cjg2.1217.
- Reddy, S. M., G. J. Potts, S. P. Kelley, and N. O. Arnaud (1999), The effects of deformation-induced microstructures on intragrain $^{40}\text{Ar}/^{39}\text{Ar}$ ages in potassium feldspar, *Geology*, *27*, 363–366, doi:10.1130/0091-7613(1999)027.
- Reddy, S. M., G. J. Potts, and S. P. Kelley (2001), $^{40}\text{Ar}/^{39}\text{Ar}$ ages in deformed potassium feldspar: Evidence of microstructural control on Ar isotope systematics, *Contrib. Mineral. Petrol.*, *141*, 186–200, doi:10.1007/s004100000227.

- Rutshtein, I. G. (Ed.) (1992), *Geological Map of the Chita Region (1:500,000)*, 23 pp., MPGIT, Moscow, Russia.
- Shao, J., L. Zhang, and B. Mu (1998), Thermo-tectonic evolution in middle and south part of Dahinggan, *Sci. China, Ser. D*, *28*, 194–200.
- Shen, C., R. A. Donelick, P. B. O'Sullivan, R. Jonckheere, Z. Yang, Z. She, X. Miu, and X. Ge (2012), Provenance and hinterland exhumation from LA-ICP-MS zircon U–Pb and fission-track double dating of Cretaceous sediments in the Jiangnan Basin Yangtze block, central China, *Sediment. Geol.*, *281*, 194–207, doi:10.1016/j.sedgeo.2012.09.009.
- Tang, Y. J., H. F. Zhang, J. F. Ying, J. Zhang, and X. M. Liu (2008), Refertilization of ancient lithospheric mantle beneath the central North China Craton: Evidence from petrology and geochemistry of peridotite xenoliths, *Lithos*, *101*, 435–452, doi:10.1016/j.lithos.2007.09.006.
- Villa, I. M. (1994), Multipath Ar transport in K-feldspar deduced from isothermal heating experiments, *Earth Planet. Sci. Lett.*, *122*, 393–401, doi:10.1016/0012-821X(94)90010-8.
- Wang, X. F., and X. H. Chen (2005), *Stratigraphy in China*, Geological Press, Beijing, China.
- Wang, Y., and H. M. Li (2008), Initial formation and Mesozoic tectonic exhumation of an intracontinental tectonic belt of the northern part of the Taihang Mountain Belt Eastern Asia, *J. Geol.*, *116*, 155–172, doi:10.1086/529153.
- Wang, J. Y., M. Chen, J. Wang, and X. Deng (1985), On the evolution of the geothermal regime of the North China Basin, *J. Geodyn.*, *4*, 133–148, doi:10.1016/0264-3707(85)90056-0.
- Wang, F., X. Lu, C.-H. Lo, F. Y. Wu, L. Yang, and R. X. Zhu (2007), Post-collisional, potassic monzonite-minette complex (Shahewan) in the Qinling Mountains (central China): $^{40}\text{Ar}/^{39}\text{Ar}$ thermochronology, petrogenesis, and implications for the dynamic setting of the Qinling orogen, *J. Asian Earth Sci.*, *31*, 153–166, doi:10.1016/j.jseas.2007.06.002.
- Wang, F., et al. (2013a), $^{40}\text{Ar}/^{39}\text{Ar}$ thermochronology on Central China Orogen: Cooling, uplift and implications for the orogeny dynamics, in *$^{40}\text{Ar}/^{39}\text{Ar}$ Dating: From Geochronology to Thermochronology, From Archaeology to Planetary Sciences, Special Publications*, vol. 378, edited by F. Jourdan, D. F. Mark, and C. Verati, Geological Society, London, London, doi:10.1144/SP378.3.
- Wang, Y., L. Y. Zhou, and L. J. Zhao (2013b), Cratonic reactivation and orogeny: An example from the northern margin of the North China Craton, *Gondwana Res.*, *24*, 1203–1222, doi:10.1016/j.gr.2013.02.011.
- Wang, Y. J., W. M. Fan, G. W. Zhang, and Y. H. Zhang (2013c), Phanerozoic tectonics of the South China Block: Key observations and controversies, *Gondwana Res.*, *23*, 1273–1305, doi:10.1016/j.gr.2012.02.019.
- Warnock, A. C., and P. K. Zeitler (1998), $^{40}\text{Ar}/^{39}\text{Ar}$ thermochronometry of K-feldspar from the KTB borehole Germany, *Earth Planet. Sci. Lett.*, *158*, 67–79, doi:10.1016/S0012-821X(98)00044-2.
- Wartho, J. A., S. P. Kelley, R. A. Brooker, M. R. Carroll, I. M. Villa, and M. R. Lee (1999), Direct measurement of Ar diffusion profiles in a gem-quality Madagascar K-feldspar using the ultra-violet laser ablation microprobe (UVLAMP), *Earth Planet. Sci. Lett.*, *170*, 141–153, doi:10.1016/S0012-821X(99)00088-6.
- Wilde, S. A., X. H. Zhou, A. A. Nemchin, and M. Sun (2003), Mesozoic crust-mantle interaction beneath the North China craton: A consequence of the dispersal of Gondwanaland and accretion of Asia, *Geology*, *31*, 817–820, doi:10.1130/G19489.1.
- Windle, B. F., S. Maruyama, and W. J. Xiao (2010), Delamination/thinning of sub-continental lithospheric mantle under eastern China: The role of water and multiple subduction, *Am. J. Sci.*, *310*, 1250–1293, doi:10.2475/10.2010.03.
- Wu, F. Y., J. Q. Lin, S. A. Wilde, X. O. Zhang, and J. H. Yang (2005), Nature and significance of the Early Cretaceous giant igneous event in Eastern China, *Earth Planet. Sci. Lett.*, *233*, 103–119, doi:10.1016/j.epsl.2005.02.019.
- Wu, F. Y., D. Y. Sun, W. C. Ge, Y. B. Zhang, M. L. Grant, S. A. Wilde, and B. M. Jahn (2011), Geochronology of the Phanerozoic granitoids in northeastern China, *J. Asian Earth Sci.*, *41*, 1–30, doi:10.1016/j.jseas.2010.11.014.
- Xu, Y. G. (2007), Diachronous lithospheric thinning of the North China Craton and formation of the Daxin'anling-Taihangshan gravity lineament, *Lithos*, *96*, 281–298, doi:10.1016/j.lithos.2006.09.013.
- Xu, Y. G., X. L. Huang, J. L. Ma, Y. B. Wang, Y. Lizuka, J. F. Xu, Q. Wang, and X. Y. Wu (2004), Crustal-mantle interaction during the thermo-tectonic reactivation of the North China Craton: SHRIMP zircon U–Pb age, petrology and geochemistry of Mesozoic plutons in western Shandong, *Contrib. Mineral. Petrol.*, *147*, 750–767, doi:10.1007/s00410-004-0594-y.
- Xu, X. S., W. L. Griffin, S. Y. O'Reilly, N. J. Pearson, H. Y. Geng, and J. P. Zhng (2007), Re–Os isotopes of sulfides in mantle xenoliths from eastern China: Progressive modification of lithospheric mantle, *Lithos*, *102*, 43–64, doi:10.1016/j.lithos.2007.06.010.
- Xu, Y. G., H. Y. Li, C. J. Pang, and B. He (2009), On the timing and duration of the destruction of the North China Craton, *Chin. Sci. Bull.*, *54*, 3379–3396, doi:10.1007/s11434-009-0346-5.
- Yang, D. B., W. L. Xu, and Q. H. Wang (2010), Chronology and geochemistry of Mesozoic granitoids in the Bengbu area, central China: Constraints on the tectonic evolution of the eastern North China Craton, *Lithos*, *114*, 200–216, doi:10.1016/j.lithos.2009.08.009.
- Yang, J. H., F. Y. Wu, S. L. Chung, S. A. Wilde, M. F. Chu, C. H. Lo, and B. Song (2005), Petrogenesis of Early Cretaceous intrusions in the Sulu ultrahigh-pressure orogenic belt, east China and their relationship to lithospheric thinning, *Chem. Geol.*, *222*, 200–231, doi:10.1016/j.chemgeo.2005.07.006.
- Yang, J. H., F. Y. Wu, S. A. Wilde, E. Belousova, and W. L. Griffin (2008), Mesozoic decratonization of the North China block, *Geology*, *36*, 467–470, doi:10.1130/G24518A.1.
- Ying, J. H., X. Zhou, and H. Zhang (2004), Geochemical and isotopic investigation of the Laiwu–Zibo carbonatites from western Shandong Province China, and implications for their petrogenesis and enriched mantle source, *Lithos*, *75*, 413–426, doi:10.1016/j.lithos.2004.04.037.
- Ying, J. F., H. F. Zhang, and Y. J. Tang (2011), Crust–mantle interaction in the central North China Craton during the Mesozoic: Evidence from zircon U–Pb chronology, Hf isotope and geochemistry of syenitic–monzonitic intrusions from Shanxi province, *Lithos*, *125*, 449–462, doi:10.1016/j.lithos.2011.03.004.
- Zhai, M. G. (2011), Cratonization and the Ancient North China Continent: A summary and review, *Sci. China Ser. D*, *54*, 1110–1120, doi:10.1007/s11430-011-4250-x.
- Zhai, M. G., R. Zhu, J. Liu, Q. Meng, Q. Hou, S. Hu, Z. Li, H. Zhang, and W. Liu (2004), Time range of Mesozoic tectonic regime inversion in eastern North China Block, *Sci. China Ser. D*, *47*, 151–159, doi:10.1360/02yd0416.
- Zhang, J., J. Xu, J. Wan, J. Zhang, and Z. W. Gao (2002), Meso-Cenozoic detachment zones in the front of the Taihang Mountains and their fission-track ages, *Geol. Bull. China*, *21*, 208–210.
- Zhang, H. F., M. Sun, X. H. Zhou, M. F. Zhou, W. M. Fan, and J. P. Zheng (2003), Secular evolution of the lithosphere beneath the eastern North China Craton: Evidence from Mesozoic basalts and high-Mg andesites, *Geochim. Cosmochim. Acta*, *67*, 4373–4387, doi:10.1016/S0016-7037(03)00377-6.
- Zhang, H. Y., Q. L. Hou, and A. Y. Cao (2007), Tectono-chronologic constraints on a Mesozoic slip and thrust belt in the eastern Jiaodong Peninsula, *Sci. China Ser. D*, *50*, 25–30, doi:10.1007/s11430-007-2073-6.
- Zhang, J., Z. F. Zhao, Y. F. Zheng, and M. N. Dai (2010), Postcollisional magmatism: Geochemical constraints on the petrogenesis of Mesozoic granitoids in the Sulu orogen China, *Lithos*, *119*, 512–536, doi:10.1016/j.lithos.2010.08.005.
- Zhao, Z. F., Y. F. Zheng, C. S. Wei, and F. Y. Wu (2011), Origin of postcollisional magmatic rocks in the Dabie orogen: Implications for crust–mantle interaction and crustal architecture, *Lithos*, *126*, 99–124, doi:10.1016/j.lithos.2011.06.010.

- Zheng, J. P., S. Y. O'Reilly, W. L. Griffin, F. X. Lu, M. Zhang, and N. J. Pearson (2001), Relic refractory mantle beneath the eastern North China block: Significance for lithosphere evolution, *Lithos*, *57*, 43–66, doi:10.1016/S0024-4937(00)00073-6.
- Zheng, J. P., W. L. Griffin, and S. Y. O'Reilly (2007), Mechanism and timing of lithospheric modification and replacement beneath the eastern North China Craton: Peridotitic xenoliths from the 100 Ma Fuxin basalts and a regional synthesis, *Geochim. Cosmochim. Acta*, *71*, 5203–5225, doi:10.1016/j.gca.2007.07.028.
- Zhu, Y. S. and J. X. Yang (1998), The characteristics of Yanahan movement in Yinshan Belt [in Chinese with English abstract], *Iner-Mongolia Geol.*, *2*, 29–37.
- Zhu, R. X., J. H. Yang, and F. Y. Wu (2012a), Timing of destruction of the North China Craton, *Lithos*, *149*, 51–60, doi:10.1016/j.lithos.2012.05.013.
- Zhu, R. X., Y. G. Xu, G. Zhu, H. F. Zhang, Q. K. Xia, and T. Y. Zheng (2012b), Destruction of the North China Craton, *Sci. China. Ser. D*, *55*, 1565–1587, doi:10.1007/s11430-012-4516-y.